UNIVERSITY OF LATVIA

Summary of Doctoral Thesis

Ilze Ošiņa

SPECTRAL LINE IMAGING FOR NON-CONTACT SKIN DIAGNOSTICS AND COUNTERFEIT DETECTION

Riga 2023

UNIVERSITY OF LATVIA

FACULTY OF PHYSICS, MATHEMATICS AND OPTOMETRY

Ilze Ošiņa

SPECTRAL LINE IMAGING FOR NON-CONTACT SKIN DIAGNOSTICS AND COUNTERFEIT DETECTION

SUMMARY OF THE DOCTORAL THESIS

Submitted for the Doctoral degree in Physics and Astronomy
Subfield of Medical Physics

Riga 2023

The doctoral thesis was carried out at the Institute of Atomic Physics and Spectroscopy of University of Latvia from 2017 to 2023.

The thesis contains the introduction, three chapters, a summary, main results and conclusions, a bibliography, additional information and acknowledgements.

Form of thesis: dissertation in Physics and Astronomy, subfield of Medical Physics.

Scientific supervisor: professor *Dr. habil. phys.* **Jānis Spīgulis**

Reviewers:

1) professor *Dr. habil. phys.* **Ruvins Ferbers**, University of Latvia
2) professor *Dr. phys.* **Aleksejs Kataševs**, Riga Technical University
3) professor *Ph.D.* **Dror Fixler**, Bar-Ilan University (Israel)

The thesis will be defended at the public session of the Doctoral Committee of Physics, Astronomy and Mechanics, University of Latvia at 15:00 on September 21, 2023.

The doctoral thesis and its summary are available at the library of the University of Latvia, Kalpaka Blvd 4, Riga.

Chairman of the Doctoral Committee: *Dr. habil. phys.* **Ruvins Ferbers**

Secretary of the Doctoral Committee: **Sintija Siliņa**

ISBN 978-9934-36-044-2
ISBN 978-9934-36-045-9 (PDF)

ABSTRACT

This work is dedicated to researching the possibilities of an innovative multispectral imaging method – spectral line imaging – for practical applications in dermatology and forensics. Prototypes of three, four and five spectral line imaging devices have been developed and successfully tested in a laboratory setting and through clinical measurements. It has been experimentally proven that the sets of spectral images obtained under the illumination of several discrete spectral lines are more useful in non-contact diagnostics of skin neoplasms than the images obtained under the illumination of narrow-band LEDs. The suitability of several modifications of the Beer-Lambert law for skin diagnostics using spectral line imaging was analyzed. Based on the results of clinical measurements, a new data 3D-representation method for the classification of skin neoplasms was proposed. A computer program for the conversion of spectral line images into distribution maps of the main skin chromophores was developed to facilitate advanced diagnostics of malignant (melanoma, basal cell carcinoma) and benign (nevus, seborrheic keratosis, hemangioma, etc.) skin formations.

Effective application of the spectral line imaging method for recognition of printed forgeries was experimentally confirmed, as well. New algorithms and criteria for detecting counterfeits have been proposed as a result of comparative measurements of real-counterfeit Euro banknotes and document samples.

The obtained results were published in 19 SCOPUS-indexed scientific articles (including five articles in Q1-journals) and four patent descriptions, they were presented in 16 reports at international conferences and seminars.

Keywords: spectral imaging, Beer-Lambert law, skin chromophore mapping, skin neoplasms, money and document forgery.

TABLE OF CONTENTS

LIST OF ABBREVIATIONS

Bil	bilirubin
BLL	Beer-Lambert law
c	concentration
Deox	deoxyhemoglobin
ε	extinction coefficient
g	anisotropy factor
HSI	hyperspectral imaging
I	light intensity
IAPS	Institute of Atomic Physics and Spectroscopy
IR	infrared
k	attenuation coefficient
l	photon path length
LED	Light emitting diode
Lip	lipids
λ	wavelengths
M	mole
Mel	melanin
MSI	multispectral imaging
μ_a	absorption coefficient
μ_{ef}	effective attenuation coefficient
μ_s	scattering coefficient
μ'_s	reduced scattering coefficient
Ox	oxyhemoglobin
RGB	red, green and blue
S	spectral sensitivity
UV	ultraviolet

1. INTRODUCTION

1.1. General introduction and motivation

Nowadays, a wide range of research methods are available for analyzing various objects – both living organisms and a wide variety of materials. Commonly used methods are often destructive and harmful to the body [1–3]. A short measurement time is important to avoid motion artifacts for *in vivo* studies. Therefore, it is necessary to develop non-invasive, informative, reliable, fast and easy-to-use methods and to explore their application possibilities.

In this context, several optical methods that do not damage the examined object are relevant, such as confocal microscopy [4], optical coherence tomography [5], Raman spectroscopy [6] and spectral imaging [7]. In multispectral and hyperspectral imaging, images of the object being studied are obtained in several spectral bands. The main disadvantages of these methods are the large amount of data with unnecessary collateral information, low spectral selectivity and possible motion artifacts since the measurement can take up to several minutes [8]. Besides, changes in the optical properties of the object within the imaged spectral bands are possible, which usually are not taken into account.

This work examines a less explored modality of spectral imaging – the acquisition and processing of spectral line images. In particular, instead of spectral band images, we focus on images related to narrow spectral lines, acquired under discrete laser spectral line illumination [9]. Consequently, the spectral selectivity of imaging and the related color sensitivity is significantly improved, and processing of the spectral image set becomes simpler and faster. In addition, several spectral line images can be taken simultaneously by a single snapshot (which solves the problem of motion artifacts): using an n-band camera, n spectral line images can be extracted from the image data [10].

1.2. Aim and objectives of the work

The **aim** of this study is to further develop the methodology of spectral line imaging and to explore the application possibilities of this technique for the diagnosis of skin malformations and banknote and document forgery detection.

The **objectives** of the study are:

1. To complement the spectral line imaging technique by creating and testing prototype devices for the simultaneous acquisition of several spectral line images and by developing software for processing spectral image sets.
2. To evaluate the potential of the multi-spectral-line imaging method and the applicability of Beer-Lambert's law for non-contact diagnostics of various skin neoplasms by performing laboratory and clinical measurements and analyzing the results.

3. To explore the possibilities of spectral line imaging for the detection of printed forgeries by comparing experimentally obtained spectral images of original and counterfeit samples of banknotes and documents.

1.3. The main thesis

1. Discrete spectral line illumination ensures more accurate data for skin diagnostics based on spectral image acquisition and diffusely reflected light analysis, if compared to the data obtained using spectral band illumination. [P2, K4]
2. For the first time, systematic studies confirmed the efficient applicability of the spectral line imaging method and modified Beer-Lambert's law for the evolution of concentration changes and distributions of specific chromophores in skin malformations. [P1, P2, P6, P7, P8, K4, K5, K8, K9, K10, K11, R1, R4]
3. The proposed innovative 3D-representation method of diffusely reflected light intensity attenuation at three wavelengths opens a new possibility for the classification of skin neoplasms (hemangiomas, nevi, seborrheic keratoses, melanomas and basal cell carcinomas). [P1]
4. The spectral line imaging method is well suited for the highly sensitive detection of printed counterfeits (banknotes and documents) by analyzing specific parameters of spectral images. [P3, K7, K8, R1, R3]
5. The developed three, four and five spectral line imaging devices are efficient tools for skin diagnostics and forgery detection. [P1, P2, P3, P5, P6, P7, P8, K2, K3, K4, K5, K6, K7, K8, K9, K10, K11, R1, R2, R4]

1.4. Scientific novelty of the work

The scientific novelty of obtained results is confirmed by 19 articles in international publications included in the SCOPUS database, as well as by four registered patents.

Four new prototypes for multi-spectral-line imaging were created and tested in this work. Original solutions for obtaining uniform illumination simultaneously by several spectral lines were proposed and patented [R2].

New options for chromophore mapping in skin neoplasms by transforming several spectral line images were explored; unconventional modifications of the Beer-Lambert law for image processing were proposed and tested.

For the first time, spectral line images of original and counterfeit EUR banknotes and documents were experimentally compared, finding significant differences in them.

1.5. Author's contribution

The author took part in the process of device development for spectral line imaging: offered various device designs and solutions for more uniform

illumination, tested the devices and recommended their improvements. Clinical measurements of skin neoplasms were carried out in cooperation with laboratory colleagues and dermatologist Anna Bērziņa of the Laserplastic Clinic. Measurements with counterfeit EUR banknotes withdrawn from circulation were carried out in cooperation with the Bank of Latvia.

The author independently performed all spectral line image measurements, researched various modifications of Beer-Lambert's law and their applicability in skin diagnostics, performed laboratory tests of skin phantoms to determine hemoglobin concentration, created and improved image processing programs in *Matlab* software, processed and analyzed the obtained data. The results were interpreted in cooperation with the supervisor. Being a co-author of 19 published papers, in five of them she is the main (corresponding) author.

1.6. Approbation of the results

The results are published in **8 scientific journals** (incl. 5 Q1 and 2 Q2):

P1. **I. Oshina**, J. Spigulis, I. Kuzmina, L. Dambite, A. Berzina, "Three-dimensional representation of triple spectral line imaging data as an option for noncontact skin diagnostics", ***Journal of Biomedical Optics***, 27(9), 095005 (2022). doi: 10.1117/1.JBO.27.9.095005

P2. I. Kuzmina, **I. Oshina**, L. Dambite, V. Lukinsone, A. Maslobojeva, A.Berzina, J.Spigulis, "Skin chromophore mapping by smartphone RGB camera under spectral band and spectral line illumination", ***Journal of Biomedical Optics***, 27(2), 026004 (2022). doi: 10.1117/1.JBO.27.2.026004

P3. T.Fischer, **I. Oshina,** et al., "Profiling and imaging of forensic evidence – A pan-European forensic round robin study part 1: Document forgery", ***Science & Justice***, 62(4), 433–447 (2022). doi:10.1016/J.SCIJUS.2022.06.001

P4. **I. Oshina**, J.Spigulis, "Beer–Lambert law for optical tissue diagnostics: current state of the art and the main limitations", ***Journal of Biomedical Optics***, 26(10), 1–17 (2021). doi: 10.1117/1.jbo.26.10.100901

P5. J. Spigulis, V. Lukinsone, **I. Oshina**, E. Kviesis-Kipge, M. Tamosiunas, A. Lihachev, "Riga Group's recent results on laser applications for skin diagnostics", ***Journal of Physics: Conference Series***, 1859(1), (2021). doi:10.1088/1742-6596/1859/1/012033

P6. J. Spigulis, Z. Rupenheits, U. Rubins, M. Mileiko, **I. Oshina**, "Spectral line reflectance and fluorescence imaging device for skin diagnostics", ***Applied Sciences*** (Switzerland), 10(21), 1–10, (2020). doi:10.3390/app10217472

P7. J. Spigulis, **I. Oshina**, A.Berzina, A.Bykov, "Smartphone snapshot mapping of skin chromophores under triple-wavelength laser illumination", ***Journal of Biomedical Optics***, 22(9), 091508 (2017). doi: 10.1117/1.JBO.22.9.091508

P8. J. Spigulis, **I. Oshina**, "Snapshot RGB mapping of skin melanin and hemoglobin", ***Journal of Biomedical Optics***, 20(5), 050503 (2015). doi: 10.1117/1.JBO.20.5.050503

The results are published in **11 full-text articles in conference proceedings** (found in the *Scopus* database):

K1. **I. Oshina**, J. Spigulis, "Potential of the Beer–Lambert law for skin chromophore mapping from diffuse reflectance images", ***Proc. SPIE*** 11920, Diffuse Optical Spectroscopy and Imaging VIII, Opt. InfoBase Conf. Pap. (2021), 119201X, 0–2, doi:10.1117/12.2615427

K2. J. Spigulis, I. Kuzmina, V. Lukinsone, M. Tamosiunas, **I. Oshina**, L. Ozolina, A. Maslobojeva, M. Kuzminskis, D. Ivanov, E. Borisova, "Towards combined multispectral, FLIM and Raman imaging for skin diagnostics", ***Proc. SPIE*** 11232, Multimodal Biomedical Imaging XV, 112320N (2020), p. 23. doi: 10.1117/12.2559107

K3. J. Spigulis, Z. Rupenheits, M. Matulenko, **I. Oshina**, U. Rubins, "A snapshot multi-wavelengths imaging device for in-vivo skin diagnostics" ***Proceedings of the Multimodal Biomedical Imaging XV***; 112320I; SPIE, (2020), doi: 10.1117/12.2547286

K4. I. Kuzmina, V. Lukinsone, U. Rubins, **I. Osina**, L. Dambite, A. Maslobojeva, J. Spigulis, "Agar-based phantoms for skin diagnostic imaging", ***Proc. SPIE*** 11363, Tissue Optics and Photonics, 113630F (2020), p. 15. doi: 10.1117/12.2555674

K5. J. Spigulis, A. Lihachev, V. Lukinsone, M. Osis, **I. Oshina**, "Lasers for in-vivo skin diagnostics: some recent developments", ***Proc. SPIE*** 11047, 20th International Conference and School on Quantum Electronics: Laser Physics and Applications, 1104703 (2019), p. 38. doi: 10.1117/12.2516747

K6. J. Spigulis, **I. Oshina**, M. Matulenko, "Laser illumination designs for snapshot multi-spectral-line imaging", Conference on Lasers and Electro-Optics Europe and European Quantum Electronics Conference, CLEO/Europe-EQEC, ***OSA Technical Digest*** (Optica Publishing Group), paper cl_3_42019, art. no. 8872998, (2019), doi: 10.1109/CLEOE-EQEC.2019.8872998

K7. **I. Oshina**, P. Potapovs, J. Spigulis, "Spectral imaging system for money counterfeit detection", Proceedings of the Optics InfoBase Conference Papers; Imaging and Applied Optics (COSI, IS, MATH, pcAOP), ***OSA Technical Digest***., (2019), doi: 10.1364/ISA.2019.ITu3B.3

K8. J. Spigulis, **I. Oshina**, P. Potapovs, K. Lauberts, "Snapshot multi-spectral-line imaging for applications in dermatology and forensics", ***Proc. SPIE*** 10881, Imaging, Manipulation, and Analysis of Biomolecules, Cells, and Tissues XVII; 10881, 1088114, (2019), doi: 10.1117/12.2508204

K9. **I. Oshina**, J. Spigulis, U. Rubins, E. Kviesis-Kipge, K. Lauberts "Express RGB mapping of three to five skin chromophores", ***Proc. SPIE*** 10413, Novel Biophotonics Techniques and Applications IV, 104130M (2017); doi: 10.1117/12.2285995

K10. J. Spigulis, **I. Oshina**, Z. Rupenheits, "Smartphone single-snapshot mapping of skin chromophores", ***Biomedical Optics 2016***, OSA Technical Digest (online), JTu3A.46 (2016), doi: 10.1364/CANCER.2016.JTu3A.46

K11. J. Spigulis, **I. Oshina**, "3×3 technique for RGB snapshot mapping of skin chromophores", Optics in the Life Sciences, ***OSA Technical Digest*** (online) (Optical Society of America), paper JT3A.39, (2015), doi: 10.1364/BODA.2015.JT3A.39

Four patent descriptions:

R1. J. Spīgulis, **I. Oši̧ņa**, I. Kuzmina, L. Dambīte, " Method and device for determination of photo-camera relative spectral sensitivity at selected wavelengths", LV 15705 B (2021).

R2. J. Spīgulis, **I. Oši̧ņa**, Z. Rupenheits, M. Matuļenko, "Device for uniform surface illumination simultaneosly by several laser spectral lines", LV 15491 B (2020).

R3. J. Spīgulis, **I. Oši̧ņa**, "Method for detection of coloured counterfeits", LV 15413 B (2019).

R4. J. Spīgulis, **I. Oši̧ņa** "Method and device for chromophore mapping under illumination by several spectral lines", LV 15106 B (2016).

The results have been publicly presented at **16 international conferences and seminars** (as the first author):

C1. "COMULIS conference" (COST action CA17121), Nicosia, Cyprus, poster presentation "Multi-spectral-line imaging of skin phantoms with tattoo ink", **I. Oshina**, J. Spigulis, 21.–22.09.2022.

C2. "WG3 Meeting - Skin Project" conference (COST action CA17121), Tel Aviv, Israel, presentation "Riga Biophotonics Laboratory and Performed There Spectral Imaging of the Skin Phantoms", **I. Oshina**, J. Spigulis, 18.–20.05.2022.

C3. "MultiForesee 2021 conference, online, poster presentation "Potential of modified Beer-Lambert law for skin bruise analysis", **I. Oshina**, J. Spigulis, 12.–14.07.2021.

C4. "European Conferences on Biomedical Optics", "Diffuse Optical Spectroscopy and Imaging VIII", online, poster presentation "Potential of the Beer–Lambert Law for Skin Chromophore Mapping from Diffuse Reflectance Images", **I. Oshina**, J. Spigulis, 20.–24.06.2021.

C5. "SPIE Optics + Photonics 2020 Digital Forum", "Novel Optical Systems, Methods, and Applications XXIII conference", online, presentation "Skin chromophore mapping from multispectral laser line images", **I. Osina**, I. Kuzmina, U. Rubins, V. Lukinsone, A. Maslobojeva, L. Dambite, M. Matulenko, Z. Rupenheits, J. Spigulis, 17.–24.08.2020.

C6. "OSA Imaging and Applied Optics Congress", "Imaging Systems and Applications", Munich, Germany, presentation "Spectral imaging system

for money counterfeit detection", **I. Oshina**, P. Potapovs, J. Spigulis, 24.–28.06.2019 .

C7. "Biophotonics and imaging graduate summer school BIGSS", Ballyvaughan, Ireland, poster presentation "Polychromatic spectral imaging for chromophore mapping and counterfeit detection", **I. Oshina**, J. Spigulis 28.08.–01.09.2018 .

C8. "World congress on medical physics & biomedical engineering" Prague, Czech Republic, poster presentation "Human iris diagnostics using double-snapshot method and spectral line imaging", **I. Oshina**, K. Lauberts, E. Kviesis-Kipge, J. Spigulis, 03.–08.06.2018.

C9. Conference "The Second Forensic Science Meeting of Trace Evidence", Riga, Latvia, presentation "Euro-banknote forgery detection at triple wavelength laser illumination", **I. Oshina**, P. Potapovs, J. Spigulis, 17.05.2018.

C10. "SPIE Photonics Europe", Strasbourg, France, two poster presentations: "A method for counterfeits detection using a smartphone camera and spectral line imaging", **I. Oshina**, P. Potapovs, J. Spigulis, and "Double-snapshot mapping of up to five skin chromophores", **I. Oshina**, R. Ciems, K. Lauberts, E. Kviesis-Kipge, J. Spigulis, 21.–26.04.2018.

C11. "European Conferences on Biomedical Optics", "Novel Biophotonics Techniques and Applications IV", Munich, Germany, poster presentation "Express RGB mapping of three to five skin chromophores", **I. Oshina**, J. Spigulis, U. Rubins, E. Kviesis-Kipge, K. Lauberts, 26.–29.06.2017.

C12. Summer school "Biophotonics '17", Ven, Sweden, poster presentation "Skin chromophore mapping and oxygen saturation measurements in human skin using polychromatic illumination", **I. Oshina**, 10.–17.06.2017.

C13. "Developments in Optics and Communications 2017", Riga, Latvia, presentation "Double-snapshot mapping of four skin chromophores", **I. Oshina**, J. Spigulis, U. Rubins, 06.–07.04.2017.

C14. "Developments in Optics and Communications 2016", Riga, Latvia, presentation "Mapping of skin chromophores by snapshot taken with a smartphone", **I. Oshina**, Z. Rupenheits, J. Spigulis, 21.–23.03.2016.

C15. "IONS Karlsruhe 2015", Karlsruhe, Germany, poster presentation "Image Processing for Snapshot RGB Mapping of Skin Chromophores", **I. Oshina**, J. Spigulis, 26.–29.06.2015.

C16. "Developments in Optics and Communications 2015", Riga, Latvia, poster presentation "Snapshot mapping of skin chromophores at triple-wavelength illumination", **I. Oshina**, J. Spigulis, 08.–10.04.2015.

2. LITERATURE OVERVIEW

2.1. Spectral imaging methods and devices

Medical imaging is often used for the diagnosis and treatment of various diseases and as additional information during operations. Magnetic resonance, X-rays, optical coherence tomography, ultrasound and other imaging methods are used. Deep learning with neural networks, support vector machines, etc. is often used together with these methods for data processing algorithms. Most of these technologies are expensive and sometimes even harmful to the human body. Therefore, relatively cheap and non-invasive imaging methods are relevant. [11]

Hyperspectral and multispectral imaging are non-contact and non-invasive methods. Images are captured in a few seconds to minutes.[8]

2.1.1. Hyperspectral imaging

Hyperspectral imaging (HSI) is the acquisition of a set of spectral images in many adjacent or even overlapping spectral bands. HSI offers a wide range of spatial and spectral information, often from the ultraviolet (UV) to infrared (IR) spectral range. The measurement results in a three-dimensional cube or hyperspectral cube. [11]

Useful information about diagnosis and treatment can be obtained for certain groups of tissues and cells from hyperspectral images. Through the measurement, very extensive information about the studied object is obtained, so data processing is advanced and time-consuming. Complications are caused by, for example, the overlapping of spectral bands and the noise of measuring instruments. Spectral images are normalized by compensating for uneven illumination and camera matrix noise [12–15]. Sometimes the most useful spectral bands for data analysis are selected to simplify calculations and reduce data processing time [16,17]. To simplify calculations, the resolution of the images is reduced, or the most important details of the images are extracted. Principal component analysis [8,18], linear discriminant analysis [19] and independent component analysis is often used for these tasks.

In medical physics, hyperspectral imaging is used in disease diagnosis, classification and segmentation. It is often combined with statistical analysis techniques such as k-nearest neighbor detection [20], linear discriminant analysis [20,21],support vector machines [20], convolutional neural networks [22,23] etc.

2.1.2. Multispectral imaging

Multispectral Imaging (MSI) uses a smaller number of separated spectral bands. The boundary between multispectral and hyperspectral imaging is not

clearly defined, some authors believe that up to 10 spectral bands are considered multispectral imaging [24], and in other cases even up to 20 bands [8], or more. A second type of division is spectral continuity: hyperspectral imaging uses a quasi-continuous spectrum, whereas multispectral imaging typically captures information in multiple non-overlapping spectral bands [25]. The multispectral dataset contains both spatial and spectral information.

Compared to hyperspectral imaging, in this case, the measurement systems can be adapted to the spectral properties of the objects being studied, such as tissue absorption properties, by choosing the most suitable wavelengths. Thus, a vector of properties characterizing the object is obtained in the measurement, instead of a full spectrum characterization. Data processing is not as complicated and time-consuming as in the case of HSI. [8]

2.1.3. Spectral line imaging

In spectral line imaging, instead of conventional spectral band images, spectral line images are obtained – images taken at fixed wavelengths. This is a relatively new imaging technology [9]. The image of the object under study is taken under the illumination of one or more narrow spectral lines, and often only one snapshot is taken with subsequent separation of the images of the individual spectral lines. Depending on how many receiving channels a digital camera has, the same number of spectral lines can be separated into images if the corresponding number of spectral lines is used for illumination [10]. It is most convenient to use laser radiation for object illumination [26]. The spectral line widths of lasers typically do not exceed 0.1 nm, and such illumination provides significantly higher imaging spectral selectivity (and therefore color sensitivity or resolution) compared to imaging in the typically >10 nm wide spectral bands used in the multi- and hyperspectral imaging discussed above. [27]

Spectral line imaging can be performed by illuminating an object simultaneously with several laser lines and analyzing the signals in each pixel of the image separately. With the help of X, Y scanners, the entire image can be scanned point by point. Another method is to perform full image measurements at successive wavelengths, but in this case, larger spectral distortions may be encountered. [28]

In the Biophotonics Laboratory of the Institute of Atomic Physics and Spectroscopy (IAPS) of the University of Latvia, the technology of imaging spectral lines was implemented for the first time in 2010 [29], by taking pictures with an RGB camera under the illumination of two laser lines (532 nm and 635 nm) for evaluating the amount of hemoglobin in the skin. In 2012, IAPS created the first prototype for providing uniform laser illumination using three laser modules (405 nm, 532 nm and 650 nm). The author got involved in research in this direction in 2014, developing master's thesis [30], and further continuing in doctoral studies. In later years, with the participation of the author, several

devices for spectral line imaging were developed, which are described in detail in section 3.1. In addition, a compact five-spectral line imaging device with 405 nm, 450 nm, 525 nm, 655 nm, and 845 nm wavelength laser diodes has been developed in the laboratory [31].

2.2. Skin structure and optical properties

In this section the focus is on the first direct application of the method – dermatology and the diagnosis of skin neoplasms. First, the structure of the skin and various neoplasms are reviewed, second, the optical properties of the skin are described – scattering, absorption and the main chromophores of the skin – and, third, the diagnostic possibilities for skin neoplasms and the creation of skin phantoms are outlined.

2.2.1. Skin structure

The skin is the largest human organ, it reflects the health and pathological processes of the body. Its basic functions are – barrier function, immunological protection, sensory function, thermoregulation, it provides water impermeability and produces vitamin D3. The skin can be divided into three layers: epidermis, dermis and hypodermis (Fig. 2.1). The main structural elements in the skin are hair roots, sweat and sebaceous glands, blood vessels and nerves. [32]

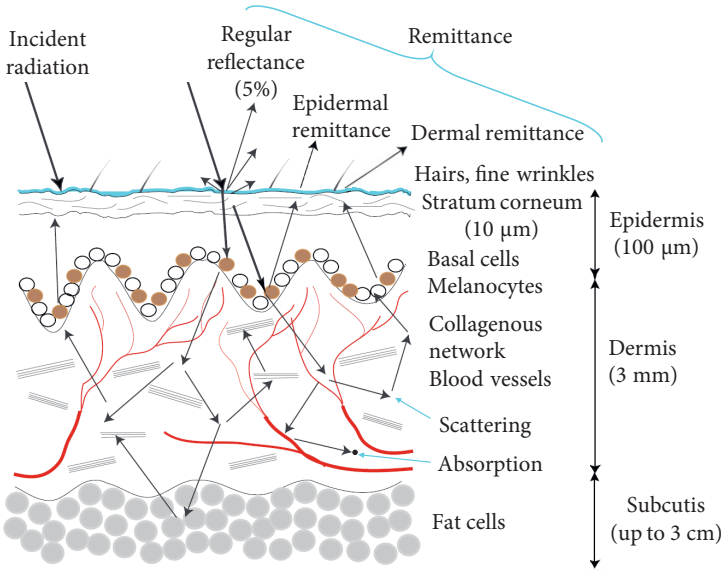

Figure 2.1 **Skin structure and interaction with light** [33,34]

The epidermis is the transparent outer layer. Its thickness ranges from 0.05 mm in the eyelids to 1.5 mm in the hands and feet, with an average of 0.1 mm. There are no blood vessels and nerve endings in it, it consists of epithelial cells also called keratinocytes. In the epidermis, the pigment melanin is produced in melanocytes. The epidermis is divided into five layers: stratum basale, stratum spinosum, stratum granulosum, stratum lucidum and stratum corneum. [32]

The thickness of the dermis or real skin is 0.5-5.0 mm. It contains blood vessels, lymphatic vessels, nerve fibers, sebaceous and sweat glands, and hair follicles. The dermis contains the proteins collagen and elastin, which make the skin firm and elastic. The superficial and deep plexus of blood vessels provides the epidermis with nutrients and regulates body temperature. The dermis can be divided into two layers: the papillary and the reticular layer. [32]

The hypodermis, or subcutaneous tissue, contains fat and connective tissue, as well as hair follicles and blood vessels. Adipose tissue is fat cells, or lipocytes, arranged in lobes, which are separated from each other by connective tissue. The hypodermis protects the body from cold and injuries and is a reservoir of nutrients. [32]

2.2.2. Skin neoplasms

The most common benign skin formations are nevi and seborrheic keratoses. Nevus is the medical term for a mole (Fig. 2.2 (a)). They occur as a result of the proliferation of pigment cells melanocytes. Nevi are most often round or oval in shape, ranging in size from a few millimeters to several centimeters. They are divided into congenital (they are present from birth) and acquired (appeared during lifetime). Nevi can also be classified by their location in the skin layers [35]:

- junctional nevi are formed on the epidermis-dermis border, they are usually flat and intensely colored;
- combined nevi are formed between the epidermis and dermis border and in the dermis when part of the nevus cells moves to lower layers of the skin; they are characterized by a raised central part with a flat pigmented band around it;
- dermal nevi are formed in the dermis, most often raised from the surface of the skin, and are pigmented or flesh-colored.

Blue nevi are usually congenital, and have a regular shape with uniform brown-blue, blue, gray-blue or gray-black pigmentation (Fig. 2.2 (b))[36].

Seborrheic keratoses appear in middle-aged and elderly people (Fig. 2.2 (c)). At the initial stage, there are small rough bumps, which thicken over time and acquire a wart-like surface. The color spectrum is from pale to brown. They can look like malignant melanoma because sometimes they are dark, irregular in shape and with uneven pigmentation. They can be difficult to diagnose. [35]

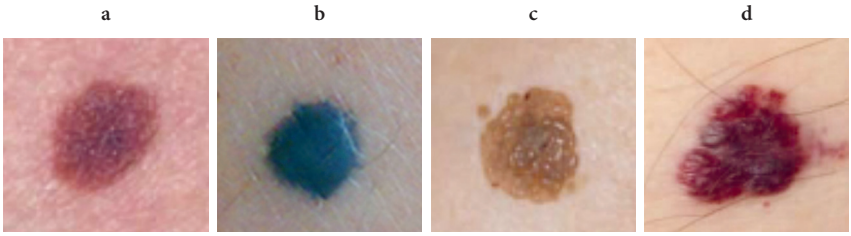

Figure 2.2 **Nevus (a), blue nevus (b), seborrheic keratosis (c), hemangioma (d)** [37,38]**.**

Hemangiomas are benign vascular formations (Fig. 2.2 (d)). They are usually round or oval in shape with reddish or purple coloration. Hemangiomas consist of dilated blood vessels in the superficial dermis. [39]

Melanoma is the most dangerous form of skin cancer, which can spread through the lymphatic vessels and cause metastases (Fig. 2.3 (a), (b)). It develops from melanocytes. In the earliest stage, they are small and irregularly shaped, and their pigmentation ranges from pink to dark brown, very similar to nevi. Later, melanomas become larger, nodular or ulcerated, and different coloring appear – brown or black with red, white or blue. [36]

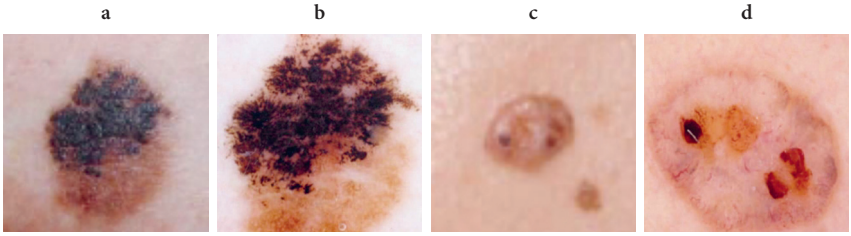

Figure 2.3 **Melanoma in daylight (a), dermatoscopically (b). Basal cell carcinoma in daylight (c), dermatoscopically (d)** [37]

Basal cell carcinoma (BCC) is the most common malignant skin tumor (Fig. 2.3 (c), (d)). It usually does not metastasize, but slowly grows larger and can grow into deeper skin structures. There are several types of basal cell carcinomas: nodular, superficial, sclerosing, and pigmented. [36]

2.2.3. Optical properties of the skin

Optical radiation is electromagnetic radiation that includes the ultraviolet (UV), visible and infrared (IR) parts of the spectrum. This radiation, when interacting with the skin, can be directly reflected from the surface of the skin or penetrate deeper into the skin tissue, where it is either completely absorbed

or, as a result of scattering, radiated back out of the tissues in diffuse reflection (Fig. 2.1) [33,34]. Approximately 4–7 % of light is reflected from the top layer of the skin, regardless of wavelength (250–3000 nm) or skin color, due to changes in the refractive index of light [34]. The path of the light beam in the skin is determined by the optical properties of the specific skin layer, which is basically influenced by the concentration of melanin, blood and keratin [40].

Scattering occurs as a result of the heterogeneity of the environment – the refractive indices differ, if the size of the particles in the environment is comparable to the wavelength of the radiation, scattering occurs on opaque tissue microstructures [34]. The main light scatterers in the skin are filamentous proteins: keratin in the epidermis and collagen in the dermis. Diffusion also occurs in melanosomes, cell nuclei, cell walls, etc. [41]

Scattering coefficient $\mu_s(\lambda)$ $[cm^{-1}]$ describes the average path length a photon must travel before it is scattered. The reduced scattering coefficient describes the extent and direction of scattering: $\mu_s' = \mu_s (1 - g)$, where g is the anisotropy factor – the average cosine of the scatterin g angle θ: $g = \langle cos\theta \rangle$. [41]

Absorption describes the reduction of light energy as it propagates through the tissue environment. As a result, the photon energy is transferred to an absorbing particle – an organic molecule or chromophore. Most of the absorbed energy is usually converted into heat and carried away by diffusion.[42]

Absorption coefficient μ_a $(\lambda)[cm^{-1}]$ describes the average path length a photon must travel through the medium before it is absorbed. The extinction coefficient $\varepsilon(\lambda)[L/mol \cdot mm]$ can also be used to characterize absorption. [43]

Light propagation in tissues (including skin) can be described by Beer-Lambert law (BLL): intensity of incident light I_0, when passing through a homogeneous layer, decreases exponentially depending on the length of the traveled path l, concentration c of absorbing substances and their extinction coefficient ε:

$$I = I_0 \cdot e^{-\varepsilon \cdot c \cdot l} \tag{2.1}$$

where I is the final intensity of the light [44,45].

Beer-Lambert law is widely used because the data processing time is short and this method is simpler than the diffusion theory [46], Monte Carlo simulation [47,48], artificial neural networks [49] and other methods. Oxygen [50] and carbon monoxide [51] saturation, oxy- and deoxyhemoglobin [52], bilirubin [53] and melanin concentration [54] can be determined using BLL.

It is assumed that the illumination is monochromatic, collimated and oriented perpendicular to the investigated surface, it is absorbed only by one type of molecules that do not interact with each other, the sample is homogeneous and there is no scattering [55]. To make the calculations more realistic, several variations of BLL have been created (Fig. 2.4). The parameters that are taken into account are – dispersion [56], absorption and the distance between the light source and the detector (modified Baer-Lambert law) [57], absorption

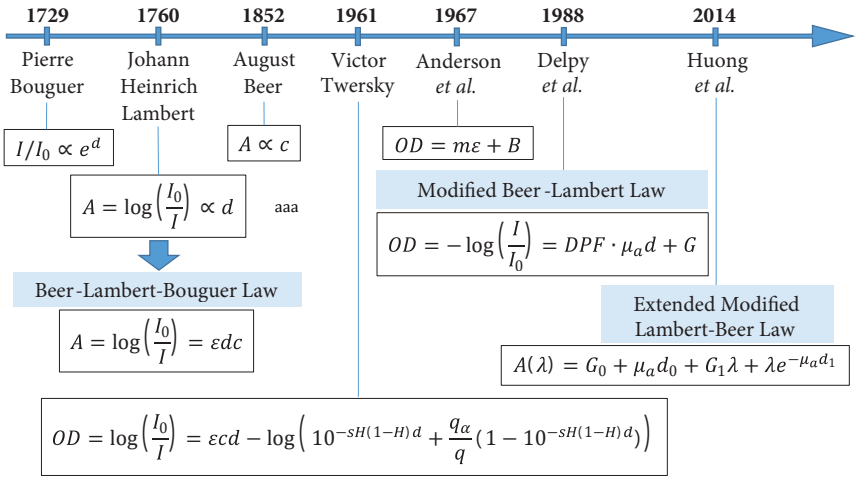

Figure 2.4 **Historical development of Beer-Lambert law** [P4]

and scattering of light in the epidermis and dermis (extended modified Lambert-Beer law) [51] etc. For the full development of the Beer-Lambert law, its various modifications, limitations and applicability, see publication P4.

2.2.4. Skin chromophores

Skin color is determined by absorption and scattering properties. Light is mostly absorbed by water molecules, proteins and skin pigments or chromophores. The main chromophores in the human skin are melanin, oxyhemoglobin and deoxyhemoglobin (Fig. 2.5). [58]

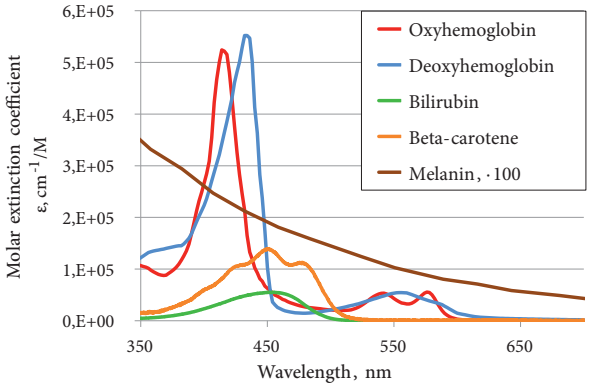

Figure 2.5 **Absorption spectra of skin chromophores** [59–62]

Melanin is produced in the epidermis in melanocytes. There are two types of melanin: brown-black eumelanin and reddish pheomelanin. The absorption coefficient of melanin decreases monotonously with increasing wavelength [32]. Hemoglobin is located in the blood and ensures the supply of oxygen in the human body. Oxyhemoglobin is hemoglobin with oxygen attached, and deoxyhemoglobin is without oxygen [59]. Bilirubin is a breakdown product of hemoglobin. Most often, bilirubin appears in bruises when extravascular erythrocytes break down [43]. Beta-carotene protects a person from excessive exposure to the sun, as it absorbs light in the ultraviolet and blue spectrum ranges. Beta-carotene is found in the bloodstream, epidermis and subcutaneous fat, and appears on the skin as a yellowish skin tone [43]. See the absorption spectra of chromophores in Figure 2.5. Lipids or body fat, scatter light well. Water weakly absorbs light in the visible part of the spectrum, but very strongly in the ultraviolet and near-infrared parts of the spectrum [43].

2.2.5. Average path of diffusely reflected photons in the skin

To determine the composition of the skin using optical methods, it is important to know the average path length of the re-emitted or diffusely reflected photons in the skin. Here two methods are discussed: using a Monte Carlo computer simulation and measuring the photon's propagation time in the skin experimentally.

Monte Carlo simulation

A Monte Carlo simulation for the case of three skin layers [P7] is described here. The first layer is the epidermis, the second is the dermis, and then there is an infinitely large layer of subcutaneous fat. The Monte Carlo simulation was performed by Alexander Bykov, a senior researcher at the Laboratory of Optoelectronics and Metrology at the University of Oulu in Finland.

To reproduce different areas of the body, the thickness of the epidermis was varied – 100, 150 and 200 μm. Dermis thickness – 1800 μm. It was assumed that the sample is uniformly illuminated by a beam with a diameter of 50 mm. The diffusely reflected photons were collected at an angle of 10 degrees. The average photon penetration depth and path length in the skin were calculated for each of the three wavelengths: 448 nm, 532 nm and 659 nm (Tab. 2.1). Calculations were made taking into account the weighted average value.

Table 2.1 **Results of Monte Carlo simulations for average photon penetration depth and path length in the skin, epidermal thickness is 0.1 mm [P7]**

Wavelength λ, nm	Average penetration depth of photons in the skin, mm	Average path length of photons in the skin, mm
448	0.18	0.92
532	0.32	1.64
659	0.76	2.98

Experimentally determined photon propagation time in the skin

The photon propagation time in the skin was measured and numerical values were calculated by Vanesa Lukinsone, lead researcher at the Institute of Atomic Physics and Spectroscopy [63]. In the experiment, a broadband picosecond laser in pulsed mode (560-800 nm) with interference filters (step between transmission peaks 40 nm) was used. Healthy forearm skin was measured. Radiation in seven narrow spectral bands was delivered to the skin with an optical fiber. The diffusely reflected signal was measured at five different distances from the excitation point: 1 mm, 8 mm, 12 mm, 16 mm and 20 mm. The average photon path length in the skin was calculated as the average value for the integrated path length distribution function (Tab. 2.2).

Table 2.2 **Average path length of diffusely reflected photons in millimeters with standard deviations for different distances between emitter and receiver** [63]

Central wavelength, nm	Distance from emitter to receiver				
	1 mm	8 mm	12 mm	16 mm	20 mm
560	16 ± 3	27 ± 3	41 ± 2	53 ± 5	62 ± 1
600	19 ± 3	37 ± 3	53 ± 4	68 ± 5	84 ± 8
640	21 ± 3	40 ± 3	59 ± 5	75 ±4	94 ± 6
680	23 ± 4	41 ± 4	64 ± 6	86 ± 10	110 ± 16
720	22 ± 2	41 ± 4	63 ± 4	85 ± 8	106 ± 12
760	22 ± 2	41 ± 3	60 ± 3	78 ± 5	96 ± 5
800	26 ± 3	42 ± 3	63 ± 4	84 ± 8	105 ± 10

2.2.6. Diagnostic options for skin neoplasms

To increase the chances of survival, early detection of malignant skin formations is very important [64]. Today, visual inspection of the skin and dermatoscopy are the gold standard for the detection of malignant skin formations. These methods are based on the competence of the doctor. During visual inspection, the diagnosis is determined using the ABCDE rule (asymmetry, border irregularities, color, diameter, evolution over time). Some melanomas can be easily detected using this method, but many early melanomas do not yet have clear ABCD signs. [65]

Dermatoscopy combines digital photography and light microscopy. The skin formation is viewed under magnification in polarized white light. Morphological structures of formations can be observed, according to which they can be classified. For suspicious formations, a biopsy is performed, or surgical excision of the formation from the skin, and histology determines whether the formation was malignant. These examinations take up to three weeks and are expensive. [36,66]

Several non-invasive optical methods for skin diagnosis have been developed, such as confocal microscopy, fluorescence imaging, optical coherence tomography, 3D topography, and multispectral and polarized imaging. In parallel with these methods, various machine learning algorithms are used to automatically classify skin neoplasms. [66]

Confocal laser scanning microscopy used *in vivo* skin diagnostics examines the skin's top layer, tissue structure, and cell cultures [4]. While used in *ex vivo* skin diagnostics, histology can be examined [67]. The *VivaScope* 1500 is a commercially available device that can distinguish melanocytes in tissues [4,65].

Three-dimensional topography imaging can provide information about the topography of the skin [66]. High-quality images are obtained in optical profilometry, but their acquisition time is very long (up to two hours) [68]. In videoscopy, two-dimensional images can be obtained for the analysis of skin texture [66]. The laser speckle method uses speckle contrast properties that depend on surface roughness, light source and detector [69].

Optical coherence tomography can obtain cross-sectional images of the skin up to a depth of two millimeters. The interference of two light waves is measured – from the reference and the reflected light off the sample. Internal structures with different refractive indices create a shift in the time of flight of photons, after which the depth of reflective tissues in the skin can be determined. [5,70]

Using optical feedback interferometry, it is possible to detect differences between healthy skin and skin with increased blood vessels, which may indicate malignancy [71,72].

Polarimetric imaging uses the polarization properties of light to detect morphological changes in tissue structures, such as the orientation of collagen fibers in different tissues [73]. Stokes and Mueller imaging is used. Stokes imaging considers four Stokes polarization parameters that fully describe the polarization of light. From these parameters, the degree of polarization, linear polarization and circular polarization, angle of linear polarization and ellipticity can be calculated, showing differences between melanomas and nevi [74–76]. Mueller matrix imaging yields a Mueller matrix with 16 elements that describe how the Stokes vector changes upon interaction with the sample [73]. The degree of polarization and angle of linear polarization show large differences between nevi and melanomas because the epidermis over melanoma is rougher than over nevi or healthy skin [74,77].

Machine learning algorithms are widely used for the diagnosis of skin cancer, analyzing digital dermatoscopy, spectroscopy, microscopy and histology images, digital photographs [78], as well as spectroscopic [79], optical coherence tomography [80] or 3D scanner (skin textures) [81] information. The tasks of the algorithms are to segment formations, distinguish dermatoscopically significant features and classify them [82]. The most

commonly used algorithms are support vector machine [80,83], k-nearest neighbors [79–81], neural networks [83,84], decision trees [84,85] and deep learning [82,86].

Multispectral imaging is widely used in skin diagnostics [66]. A series of images of different spectral bands is taken, which provides information on the skin structure down to a depth of 2 mm [65]. *SIAscopy* is a spectrophotometric intracutaneous analysis method. Eight narrow-band spectral images are obtained, which after processing provide information on the amount of collagen, hemoglobin and melanin, as well as the distribution of melanin in the epidermis and dermis [65]. *MoleMate*, using multispectral digital dermatoscopy and computer analysis, determines whether the formation is benign or requires additional examinations [87]. With *MelaFind*, 10 images are obtained in the visible and near-infrared parts of the spectrum. Based on the calculated numerical values, it is determined whether the formation is potentially malignant [65].

Other devices for detecting melanoma: *SolarScan* (dermatoscopy images processed with computer algorithms) [88,89], *FotoFinder Moleanalyzer Pro* (deep learning algorithms for structural property studies) [90], *DermaScan C* and color dopplerography (high resolution ultrasound) [65,91], *Verisante Aura* (Raman Spectroscopy) [90], *MoleMaxII* (dermatoscopy) [65], *Dermagraphix* (full body imaging) [65].

2.2.7. Skin phantoms

The main goals of creating skin-imitating phantoms are to test models and simulations in practice, test and calibrate instruments, and compare results between different laboratories. [92]

Various materials with appropriate absorption and scattering properties can be used as a basis for skin phantoms. Basic materials for phantoms [92,93]:

- Water-based liquid phantoms. They absorb light in the infrared spectrum; the necessary chromophores can be added to simulate the desired tissue.
- Hydrogel-based phantoms such as agar and gelatin. Organic molecules and cellular components can be placed in such phantoms. They mimic the elasticity and thermal properties of human tissue well. Agar can be used as a substitute for water in tissue phantoms because it has almost the same linear attenuation coefficient as skin. [94]
- Other phantoms are also available, such as phantoms from a heterogeneous lipid solution, polyester and polyurethane resins, polyvinyl alcohol gels and ex vivo tissue phantoms, engineered tissues, phantoms made of dough, metal or textile, etc.

The most commonly used light scatterers are intralipid, polystyrene microspheres, titanium dioxide, aluminum oxide and barium oxide powders [92,95].

2.3. Forgeries of money and documents

2.3.1. Counterfeit money and methods of its detection

According to the European Central Bank, 347,000 counterfeit EUR banknotes were withdrawn from circulation in 2021 [96], in 2022 this rose to 376,000 EUR banknotes [97]. At least 15-20 million EUR are counterfeited every year, and, as counterfeiting technologies develop, their detection becomes more difficult. In Latvia, 26.5% more banknotes were counterfeited in 2022 than in 2021. The most frequently counterfeited are 20 and 50 EUR banknotes. 500 EUR banknotes are professionally forged, so since 2019 they are no longer printed, but the banknotes in circulation are still valid. [98]

In order to protect the economy of the European Union and the loss of many millions of EUR, various banknote security elements and advanced counterfeit detection devices are being developed. Security elements incorporated into EUR banknotes are cotton paper, raised print (can be felt by touch), see-through image, watermark (Portrait of Europe), security strip, holographic strip, iridescent strip, optically variable color, microtext, luminescent images under ultraviolet light and security fibers [99]. The banknotes bear the signature of a former or current president of the European Central Bank: Willem F. Duisenberg, Jean-Claude Trichet, Mario Draghi or Christine Lagarde (Fig. 2.6) [100].

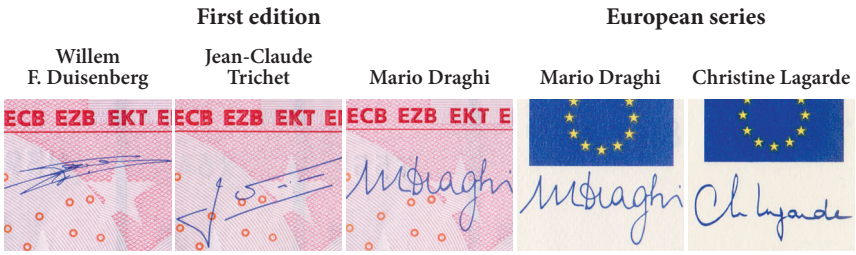

Figure 2.6 **Signatures on EUR banknotes** [100]

Banknote recognition devices are used to determine their authenticity and value. In such devices, it should be taken into account that the banknote may be damaged as a result of general use, for example, smudged or torn. In general, counterfeits look the same as authentic banknotes in visible light [101]. To start, general banknote parameters have to be checked, then the validity of the serial number is checked, which is unique for each banknote [102]. Counterfeit detection machines are either very accurate but expensive (automated teller machine) or relatively cheap and equipped with motors that direct the banknote into a dark area, where it is analyzed with light emitters and sensors. The mechanical parts of such equipment wear out over time. [101]

Steps to verify the authenticity of a banknote: take a photograph of the banknote (in illumination that allows one to distinguish its details), pre-processing the image (convert it to a black and white image, determine the borders of the banknote, segment the image), separate the necessary elements, classify the banknote and identify the currency, verify its authenticity [103]. Neural networks, Euclidean classifiers, support vector machines, k-means classifiers, etc. are used to detect and classify counterfeit banknotes. [102].

2.3.2. Forgeries of documents and their detection methods

Paper documents that are fully or partially handwritten using ink, such as certificates, wills, passports, loan agreements and other official documents, are very important in forensics. The inks and toners used in them (their source, whether one ink is used throughout the whole document, etc.), the overlaps of drawn lines, their sequence and the age of the text, as well as the paper used, can be analyzed. [104–108]

Several types of ink can be distinguished according to their dye, type of solvent (aqueous or organic) and consistency (liquid or in the form of a paste). Many inks also contain additional chemicals such as fatty acids, emulsifiers, plasticizers, and polymer resins. Usually, ink analysis is performed by combining several methods. At first, the documents are examined by non-destructive optical and visual methods, then by destructive methods. [109]

The officially recognized method for determining the type of ink is thin-layer chromatography, for which an extensive database has been created [110–112]. Gas and high-performance liquid chromatography are also used [113]. A stereomicroscope [106], UV-visible light spectrophotometry [112,114], luminescence ink spectrometry and stereomicroscopy [115–117] can be used to visually evaluate the ink. Multi- and hyper-spectral imaging can be used to determine chemical composition [118,119]. The composition of ink base substances and dyes can be determined using IR spectroscopy. For spectral methods, the spectrum of the object is compared to the database spectra or several spectra are compared to each other to make conclusions, choosing the parameters that reveal the inconsistencies of the analyzed inks [120,121]. Chemical multivariate analysis such as principal component analysis and linear discriminant analysis is also used to make an objective decision about the similarity between the two ink samples [122].

Mass spectrometry is one of the most commonly used methods to determine the compounds in the sample, such as polymers, alcohols, dyes, etc. In addition, various statistical and analytical methods can be used [108,123]. Other methods used for analysis include Raman spectroscopy [116], laser-induced breakdown spectroscopy [2], chemical imaging [124], energy dispersive X-ray fluorescence [125], total reflection X-ray fluorescence spectrometry [3], spectrofluorometry [126] etc.

As the availability and quality of printers improve, the number of counterfeits increases. Both inkjet and laser printers are analyzed [108]. The type of used paper and toner, as well as its application method and magnetic properties are determined for photocopy analysis [127].

Similar to the analysis of pen inks, for printed texts spectrometric techniques that do not damage the sample, such as IR and Raman spectroscopy, are used, which have databases created for them [128]. Polymer compound types can be determined using diffuse reflectance UV-visible light spectroscopy combined with analytical multifactorial analysis techniques [128], or laser-induced breakdown spectroscopy [129]. Prints from laser printers can be distinguished using stereomicroscopy [115].

3. METHODOLOGY

3.1. Experimental devices

During the entire study, seven laser line illumination devices were created and tested: two three laser line, three four laser line and two five laser line illumination devices. Four recent prototypes are shown in this section. For information on the first prototype of the three laser line illumination device and the results obtained, see publications P8 and K11, for the first prototypes of four and five laser line illumination devices, see publications K6, K8, K9 and [30].

3.1.1. Three laser line illumination device

The three laser line illumination device was developed at the Institute of Atomic Physics and Spectroscopy [130]. Its original application is the mapping of skin chromophores, therefore lasers with wavelengths that best represent the diversity of absorption spectra of the chromophores under study are chosen for illumination: 448 nm, 532 nm and 659 nm.

Figure 3.1 (a) shows the path of optical beams in the device and (b) its visual appearance. There are six laser modules arranged in a circle, two of each wavelength type. The laser beams are directed upwards to the reflecting disk (reflector) and are reflected from the conical edge of the organic glass disk, which forms an angle of 45° with the optical axis, and then are directed to the center of the disk. They are then dispersed downwards in an annular diffuser made of translucent plexiglass. The reflective element is covered with an aluminum film from above. The radiation is directed to the investigated surface through the first polarizer. The image of the sample is captured by a smartphone camera, with a second polarizer in front of it, directed in a perpendicular direction to the first one, to exclude the registration of the light reflected from the surface.

Figure 3.1 **Optical beam in the illumination device of three laser lines (a), the external appearance of the device in a set with a smartphone (b)** [P1, K6, K7, K8, K9]

The results and measurements made with the three laser line illumination device have been published in articles P1, P2, P7, K2, K5, K6, K7, K8, K9, K10.

3.1.2. Four laser line illumination device with two cameras

The design and external appearance of the device can be seen in Figure 3.2. Both cameras are pointed toward a circular target with a diameter of 30 mm. The RGB laser module (450 nm, 523 nm and 638 nm) and the 850 nm laser module are transmitted from each respective end into an elliptical side-emitting optical fiber. In this way, the sample is uniformly illuminated with spectral lines of four different wavelengths [R2].

During the measurement, both cameras are turned on and the device is placed over the studied object. One or more images are taken depending on the selected operating mode. All images after measurements can be viewed on the device screen, as well as transferred to an external computer for further image processing. Using the touch screen, notes can be made for each measurement individually, for example, patient information can be added for skin neoplasms.

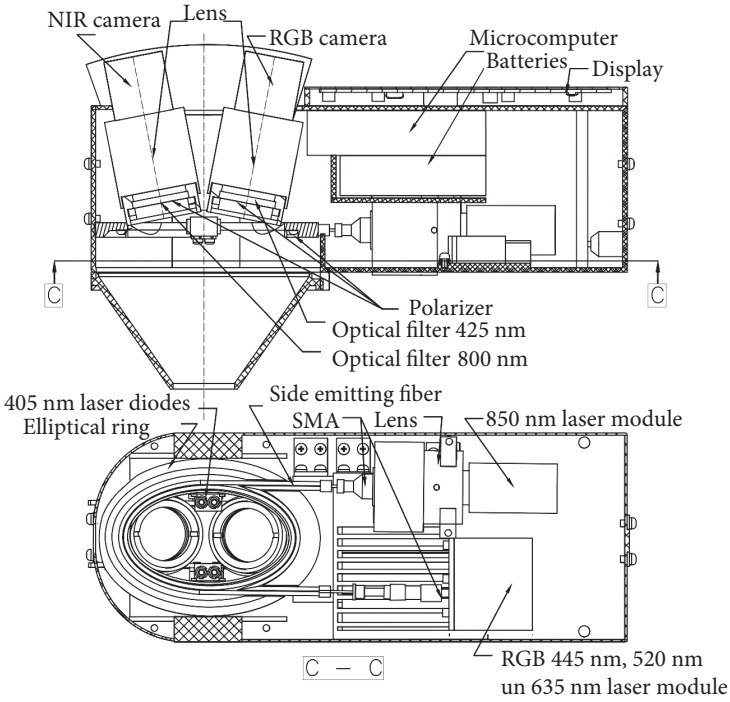

Figure 3.2 **Construction of a four laser line illumination device with two cameras** [P5, K3]

3.1.3. Four laser line illumination device with one camera

The construction of a four laser line illumination device with one camera is shown in Figure 3.3. The main difference from subsection 3.1.2. is that this device uses a four-band RGB and near-infrared spectrum camera instead of two cameras to capture images. The device uses two laser modules: RGB, which simultaneously emits three spectral lines (450 nm, 523 nm and 638 nm), and an 850 nm laser module. Both laser modules with SMA ends are connected in a spiral side-emitting optical fiber with a 400-micron silicon dioxide core, which provides uniform illumination of the sample [R2]. A polarizer for visible and near-infrared light is placed in front of the emitter. The device has replaceable round soft tips that are internally coated with a black film to avoid unwanted internal reflections. A second orthogonally oriented polarizer for visible and near-infrared light is placed in front of the camera. The images are thus stored in a microcomputer and transferred via Wi-Fi to an external computer, where they are further processed.

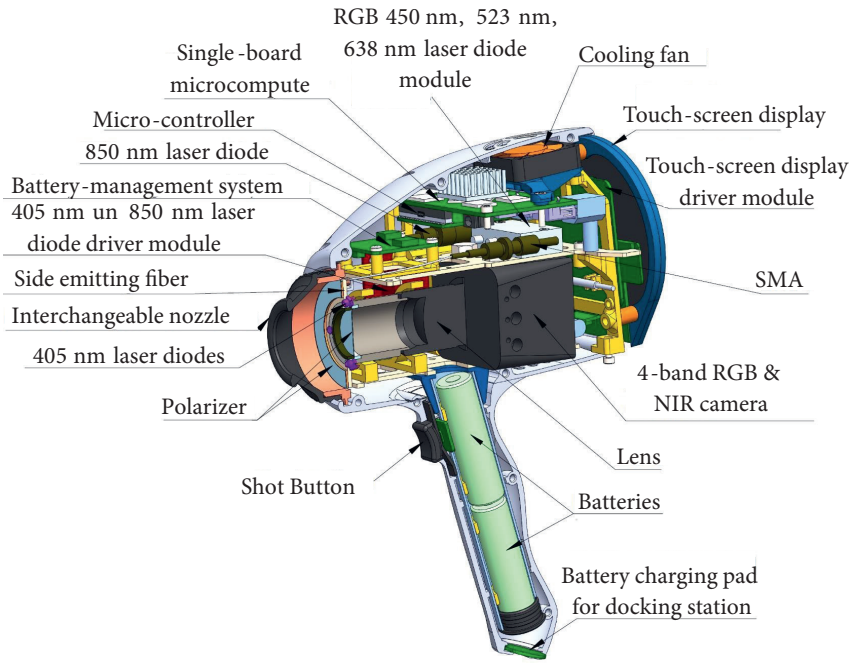

Figure 3.3 **Construction of a four laser line illumination device with one camera** [P6]

The external appearance of the four laser line illumination devices can be seen in Figure 3.4.

Figure 3.4 **The visual appearance of a four laser line illumination device with two cameras (a) and one camera (b)** [P6, K3]

3.1.4. Five laser line illumination device

For testing purposes, a five laser line illumination device was also created with laser diodes of five different wavelengths: 405 nm, 450 nm, 525 nm, 656 nm and 850 nm (Fig. 3.5). IAPS's patented technology is used for laser speckle removal [131], based on a vibrating speaker membrane (400 Hz). A diffuser is used for more even illumination. To avoid directly reflected light, two perpendicularly oriented polarizers are used. Four laser diodes are used for each wavelength arranged in a circle with the camera in the center of the device to ensure uniform illumination of the sample. For precise aiming at the sample white LEDs are used. Imaging is done with a camera that captures light in the visible and infrared spectrum ranges. Images can be viewed on a touch screen.

At the beginning of the measurement, the white LEDs are turned on, which automatically are turned off before the measurement. During measurement, two consecutive images are taken: the first image is taken under the illumination of laser diodes of wavelengths 450 nm, 525 nm and 849 nm, and the second – 405 nm and 656 nm.

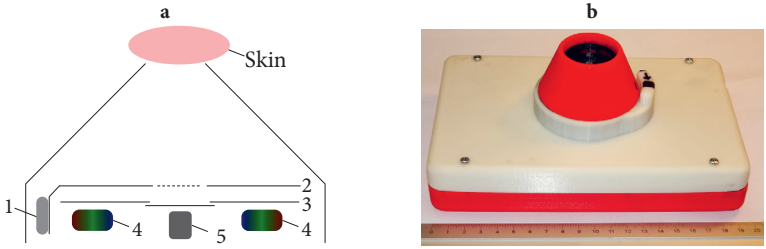

Figure 3.5 **Scheme of the optical system of the five laser line illumination device (a): loudspeaker (1), diffuser (2), cross-positioned polarizers (3), illumination ring of five wavelength laser diodes and white LEDs (4), camera (5); and the visual appearance of the device (b)** [K8]

3.2. Spectral line image processing

3.2.1. Image processing for chromophore concentration calculation

Image processing is similar for all devices. Here we will consider the three laser line illumination device case.

The image processing scheme is shown in Figure 3.6. During the measurement, only one image is taken when all three lasers are switched on simultaneously. This single image is then split into three images – one for each used wavelength using the RGB crosstalk correction algorithm (see subsection 3.2.2). Next, the images are segmented to separate the healthy skin from the skin neoplasm. From the segmented healthy skin, the average values at each of the used wavelengths (I_0) are calculated, these values reflect the basic values of the skin – reference values when there is no additional absorption in the skin, as it is in the skin neoplasms. The spectral images (I) are then divided by the reference values, yielding three attenuation coefficient maps ($k(\lambda) = I / I_0$). These coefficients are used for chromophore map calculations.

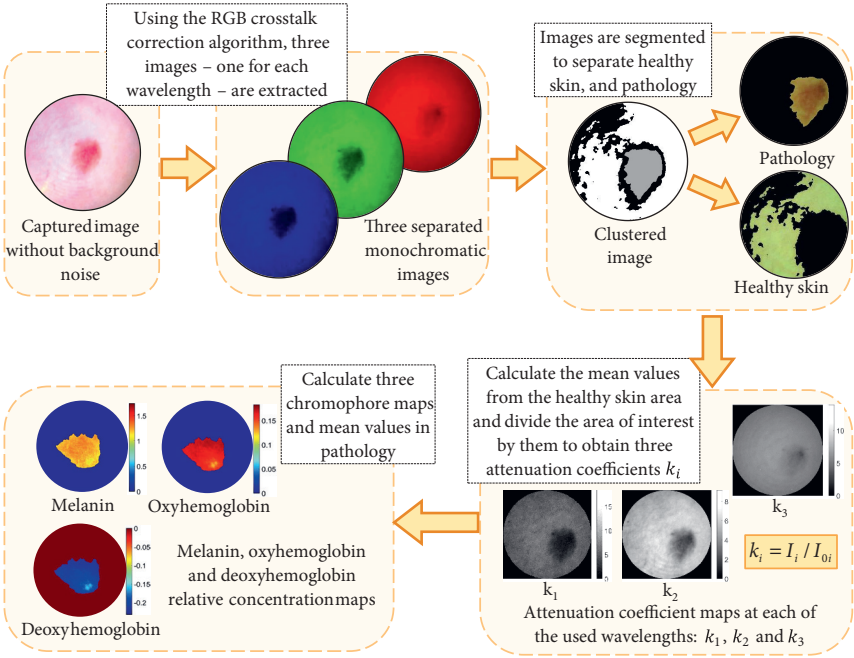

Figure 3.6 **Image processing scheme for chromophore map calculations** [P1]

3.2.2. RGB crosstalk correction algorithm

To analyze the absorption properties of an object, it is important to know the spectral attenuation coefficient k:

$$k = \frac{I}{I_0} \tag{3.1}$$

where I_0 is the incident light intensity and I is the reflected light intensity at a fixed wavelength.

The light intensity can be determined using an RGB color sensor, which registers it in three channels: red (R), green (G) and blue (B). To calculate the attenuation coefficients for the three spectral lines used for illumination, it is enough to take two images: one reference image and another image with the object and apply the RGB crosstalk correction algorithm [26].

From the spectral sensitivity curves of the camera matrix, the spectral sensitivity values of each wavelength used for illumination in each receiving channel are determined: $S(B_1)$, $S(G_1)$, $S(R_1)$, $S(B_2)$, $S(G_2)$, $S(R_2)$, $S(B_3)$, $S(G_3)$ and $S(R_3)$ (Fig. 3.7). Here, the numbers 1, 2, and 3 represent the three different wavelengths corresponding to the spectral lines used for illumination, while the symbols R, G, and B represent the three channels of the camera. If a graph of the spectral sensitivity curves of the camera matrix is not available, then the method to determine the relative spectral sensitivity of the camera at selected wavelengths can be used (see registered invention R1).

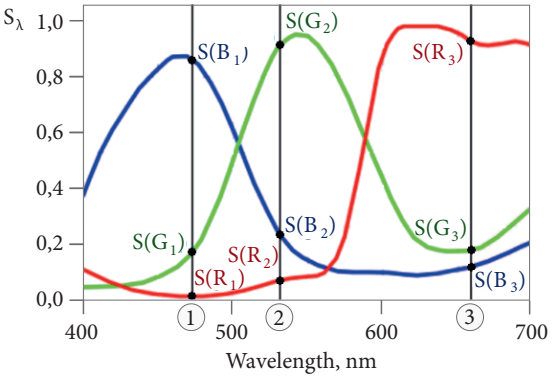

Figure 3.7 **Relative sensitivity curves of the camera matrix and marked three wavelengths (1, 2 and 3) and the spectral sensitivity values in each channel for each wavelength – $S(B_1)$, $S(G_1)$, $S(R_1)$, $S(B_2)$, $S(G_2)$, $S(R_2)$, $S(B_3)$, $S(G_3)$ and $S(R_3)$** [30]

If all light sources used for illumination have the same intensity, then the ratio of their spectral sensitivities is constant and can be expressed as $S_{Rij} = \frac{S(R_i)}{S(R_j)}$, where i and j are the wavelengths (hereafter, the equations are

described for the *R* channel, but the same relations hold for the *G* and *B* channels as well).

In the case of three different spectral lines, the values that each channel of the camera will provide is the sum of the values given by each spectral line separately: $R = \sum_{i=1}^{3} R_i$, where *i* is the wavelength.

If all light sources have the same intensity and a white reference is illuminated, then the equation holds:

$$R_i = \frac{R}{1+\frac{1}{S_{Rij}}+\frac{1}{S_{Rik}}} \tag{3.2}$$

where *i*, *j* and *k* are wavelengths.

If an object is illuminated instead of the white reference, then the reflected light of different light sources can be attenuated more or less depending on the wavelength of the spectral line. In this case, the values detected by the camera in each channel can be expressed as: $R = \sum_{i=1}^{3} k_i \cdot R_i$, where k_i is the spectral attenuation coefficient for the wavelength *i*.

Knowing the values of each channel from the white reference measurements, a system of linear equations can be derived with the three unknown attenuation coefficients. See formula derivations in the dissertation.

Similarly, four / five attenuation coefficients can be calculated if the object is illuminated by four / five spectral lines of different wavelengths, respectively, and the image is captured using a four / five channel camera.

3.2.3. Calculation of chromophore maps

A modified Beer-Lambert law was used for the calculations of the chromophore maps. Depending on the number of spectral lines used for illumination, the same number of different chromophore values can be calculated for each measurement. Here are the four variations used in the calculations.

The first model. Only melanin, oxyhemoglobin and deoxyhemoglobin are assumed to absorb light in the skin. Scattering of light in the skin is not directly considered, as the diffusely reflected light from healthy skin and skin neoplasm are compared, and the light scattering properties are assumed to be the same.

$$c_{Mel} \cdot \varepsilon_{Mel}(\lambda) + c_{Ox} \cdot \varepsilon_{Ox}(\lambda) + c_{Deox} \cdot \varepsilon_{Deox}(\lambda) = \frac{\ln(I_0(\lambda)/I(\lambda))}{2.303 \cdot l(\lambda)} \tag{3.3}$$

where *Mel* – melanin, *Ox* – oxyhemoglobin, *Deox* – deoxyhemoglobin, ε – extinction coefficient, *c* – concentration of chromophores, I_0 – intensity of light reflected from the healthy skin, *I* – intensity of light reflected from the skin neoplasm, *l* – average photon path length in the skin.

The second model. An additional variable is introduced – the loss coefficient (*z*), which characterizes the absorption of light due to other chromophores. It is also taken into account that light of different wavelengths penetrates to different depths in the layers of the skin. The depth of light penetration into

the skin is divided into two parts – part of the light is absorbed in the epidermis (melanin) and part of the light is absorbed in the dermis (oxyhemoglobin and deoxyhemoglobin).

$$c_{Mel} \cdot \varepsilon_{Mel}(\lambda) \cdot e_d(\lambda) + \left(c_{Ox} \cdot \varepsilon_{Ox}(\lambda) + c_{Deox} \cdot x(\lambda)\right) \cdot \left(1 - e_d(\lambda)\right) + z(\lambda) = \frac{\ln(I_0(\lambda)/I(\lambda))}{2.303 \cdot l(\lambda)} \tag{3.4}$$

where $z = 0{,}01 \cdot (1 - k)$ is the loss coefficient, $k = I/I_0$, e_d is part of the light that is absorbed only by the epidermis, $e_d \in [0,1]$.

The third model. The absorption coefficient is replaced by the effective attenuation coefficient $\mu_{ef} = \sqrt{3\mu_a(\mu_a + \mu_s')}$.

$$c_{Mel} \cdot \varepsilon_{Mel}(\lambda) \cdot \sqrt{1 + \frac{\mu_{s_1}'(\lambda)}{\mu_{a_1}(\lambda)}} \cdot l_1(\lambda) + \left(c_{Ox} \cdot \varepsilon_{Ox}(\lambda) + c_{Deox} \cdot \varepsilon_{Deox}(\lambda)\right) \cdot \sqrt{1 + \frac{\mu_{s_2}'(\lambda)}{\mu_{a_2}(\lambda)}} \cdot l_2(\lambda) = \frac{\ln(I_0(\lambda)/I(\lambda))}{\sqrt{3} \cdot 2.303} \tag{3.5}$$

where μ_s' is the reduced scattering coefficient, μ_a is the absorption coefficient.

The fourth model. The skin is modeled in five layers: epidermis, papillary dermis, superficial vascular network, reticular dermis, and deep vascular network. Interlayer reflection of light is also taken into account.

$$c_{Mel} \cdot \varepsilon_{Mel}(\lambda) \cdot \sqrt{1 + \frac{\mu_{s_1}'(\lambda)}{\mu_{a_1}(\lambda)}} \cdot l_1(\lambda) + \left(c_{Ox} \cdot \varepsilon_{Ox}(\lambda) + c_{Deox} \cdot \varepsilon_{Deox}(\lambda)\right) \cdot B(\lambda) = \frac{\ln(I_0(\lambda)/I(\lambda) \cdot Nn)}{\sqrt{3} \cdot 4.606} \tag{3.6}$$

where $B(\lambda) = \sum_{n=2}^{5} \sqrt{1 + \frac{\mu_{s_n}'(\lambda)}{\mu_{a_n}(\lambda)}} \cdot l_n(\lambda)$, Nn is the interlayer reflection coefficient.

In the case of a four laser line illumination device, it is possible to calculate the relative concentration of four different chromophores: melanin, oxyhemoglobin, deoxyhemoglobin and bilirubin (*Bil*), subcutaneous fat (*Lip*) or beta-carotene.

$$c_{Mel} \cdot \varepsilon_{Mel}(\lambda) + c_{Ox} \cdot \varepsilon_{Ox}(\lambda) + c_{Deox} \cdot \varepsilon_{Deox}(\lambda) + c_{Bil} \cdot \varepsilon_{Bil}(\lambda) = \frac{\ln(I_0(\lambda)/I(\lambda))}{2.303 \cdot l(\lambda)} \tag{3.7}$$

A five-laser line illumination device uses 5 lasers, so the concentrations of five different chromophores can be determined:

$$c_{Mel} \cdot \varepsilon_{Mel}(\lambda) + c_{Ox} \cdot \varepsilon_{Ox}(\lambda) + c_{Deox} \cdot \varepsilon_{Deox}(\lambda) + c_{Bil} \cdot \varepsilon_{Bil}(\lambda) + c_{Lip} \cdot \varepsilon_{Lip}(\lambda) = \frac{\ln(I_0(\lambda)/I(\lambda))}{2.303 \cdot l(\lambda)} \tag{3.8}$$

The equations described above are valid for each wavelength used in the measurement, so, for example, in the case of three wavelengths, a system of three equations is obtained with three unknown values – three chromophore concentrations. The light intensity values from the healthy skin and the skin

formation are read from the measurement images. For the average photon path length in the skin, the values calculated in the Monte Carlo simulation or the values determined from the measurements of the photon time of flight in the skin are used (see subsection 2.2.5).

3.3. Skin phantom preparation

Skin phantoms were created from agar, intralipid, lyophilized human hemoglobin powder, and water. Agar hydrogel was created by mixing agar powder with tap water and heating it. Intralipid was added to the solution to reproduce the scattering properties, and hemoglobin to reproduce the absorption properties. 0.9 to 3.3 cm high and 5 cm wide monolayer skin models with different hemoglobin concentrations were created (Fig. 3.8 (a-c)). Vascular neoplasms were simulated by adding a few drops of hemoglobin to the phantoms (Fig. 3.8 (d)). Blood vessels were imitated in a two-layer model: channels for hemoglobin water solution were carved in a 1 cm thick bottom layer, and the thickness of the upper layer was 2 mm (Fig. 3.8 (e)). Schematic images of the phantoms are shown in Figure 3.9.

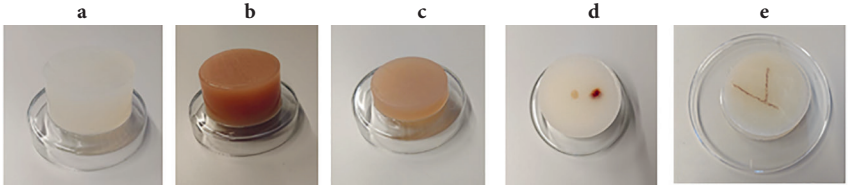

Figure 3.8 **Agar phantom (a), phantom with 3% hemoglobin and 1% intralipid (b), phantom with 1% hemoglobin (c), phantom with simulated vascular neoplasm (d), two-layer phantom with simulated blood vessel (e)** [K4]

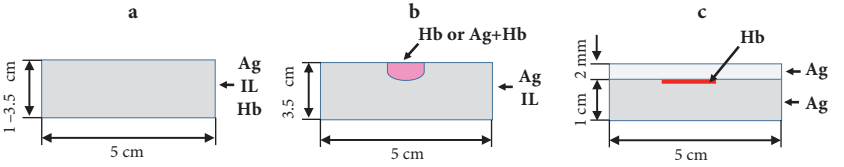

Figure 3.9 **Three types of skin phantoms: single-layer phantoms with different concentrations of intralipid and hemoglobin (a), phantoms with simulated vascular neoplasms (b) and two-layer phantoms with simulated blood vessels (c), *Ag* – agar, *IL* – intralipid, *Hb* – hemoglobin**

To compare the accuracy of the spectral band and spectral line imaging results, measurements were made with a three laser line illumination device and a spectral band device, which is basically the same, only a LED ring was

used for illumination instead of lasers (spectrum peaks – 460 nm, 535 nm and 663 nm) [P2]. Measurements were made in both transmitted and diffusely reflected light.

The following formulas were used to calculate hemoglobin concentration and extinction coefficient:

$$c = \frac{\ln\left(\frac{I_0}{I}\right)}{l \cdot \varepsilon \cdot 2{,}303} \tag{3.9}$$

$$\varepsilon = \frac{\ln\left(\frac{I_0}{I}\right)}{l \cdot c \cdot 2{,}303} \tag{3.10}$$

where I_0 is light intensity from a skin phantom made of agar and intralipid (without hemoglobin).

3.4. Samples of money and document forgeries

3.4.1. Samples of counterfeit money

In cooperation with the Bank of Latvia, measurements were made on counterfeit EUR banknotes that were withdrawn from circulation. Nine authentic and 20 counterfeit 20 EUR banknotes, 18 authentic and 11 counterfeit 50 EUR banknotes and two authentic and four counterfeit 500 EUR banknotes were analyzed. A three laser line illumination device was used for the measurements.

First, one snapshot is taken with the authentic banknote and one with the banknote to be verified. The obtained images are equalized by size and brightness and divided into three spectral line images at each of the wavelengths used for illumination, applying the RGB crosstalk correction algorithm. The significant objects are selected from the images, and the correspondence of the pixel value of the object of the banknote to be checked is compared to the values provided by the authentic banknote, both the direct values and their various relationships. A decision is made on whether the banknote being examined is authentic or counterfeit. A full description of the method is published in patent R3.

In this work, the potential areas of EUR banknotes that could be used for the implementation of the previously described authenticity verification method were analyzed.

3.4.2. Samples of forged documents

Within the framework of the COST action CA16101 "Multi-modal imaging for forensic science evidence", studies on document forgery were carried out. Potentially fake documents consisting of three pages were created in the forensic laboratory of the Portuguese police. Identical samples were sent to 17 laboratories in 16 different countries.

The study simulated a suspected intentional manipulation of a real estate rental agreement. The aim was to determine which printing technique was used,

whether a single printer was used to print all the pages, whether all the pages are of the same paper, whether they were all originally stapled together, whether the signatures were made with the same ink pens, and whether all the pages were printed and signed at the same time.

The printed text was produced by a monochromatic electrophotographic process (using a laser printer). The second page was printed using a different printer on a different type of paper in comparison to the first and third pages. There were additional paperclip marks on the first and third pages that were not visible on the second page.

The pen-written texts on the second page used a different ink than the first and third pages. The signatures on the second page were made five days later than on the first and third pages.

4. RESULTS

4.1. Diagnostic imaging of skin neoplasms

All clinical measurements were carried out with ethical approval under the supervision of dermatologist Anna Bērziņa. The measurements were performed both in the Laser Plastic Clinic at Baznīcas Street 31 and in the UL House of Science at Jelgavas Street 3.

4.1.1. Comparison of spectral line and spectral band measurements

In this subsection results obtained with the spectral band device, which uses LEDs with spectral peaks at 460 nm, 535 nm, and 663 nm for illumination, will be compared with results obtained with the spectral line device – the three laser line illumination device described in subsection 3.1.1. 105 different neoplasms were analyzed: pigmented formations (19 junctional nevi, 23 dermal nevi, 19 combined nevi), vascular formations (21 hemangiomas), as well as 23 seborrheic keratoses.

Figure 4.1 shows examples of RGB images of a hemangioma obtained with a spectral band device and a three laser line illumination device, as well as segmented chromophore maps. The relative values of the chromophore concentration maps are calculated in millimoles. The chromophore value of the surrounding healthy skin is zero, as changes in chromophore concentrations in the neoplasms are measured. In hemangioma increased oxyhemoglobin and reduced deoxyhemoglobin concentrations are observed. More pronounced changes can be observed with the spectral line device.

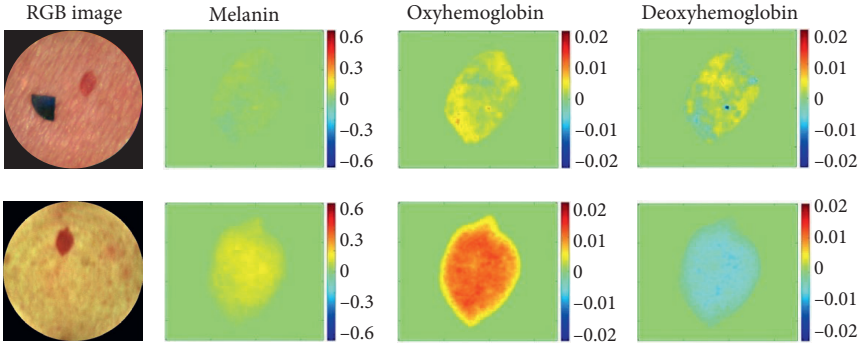

Figure 4.1 **RGB images of a hemangioma and calculated chromophore concentration maps obtained using the spectral band device (top row) and the spectral line device (bottom row). Scale values in millimoles (mM)** [P2]

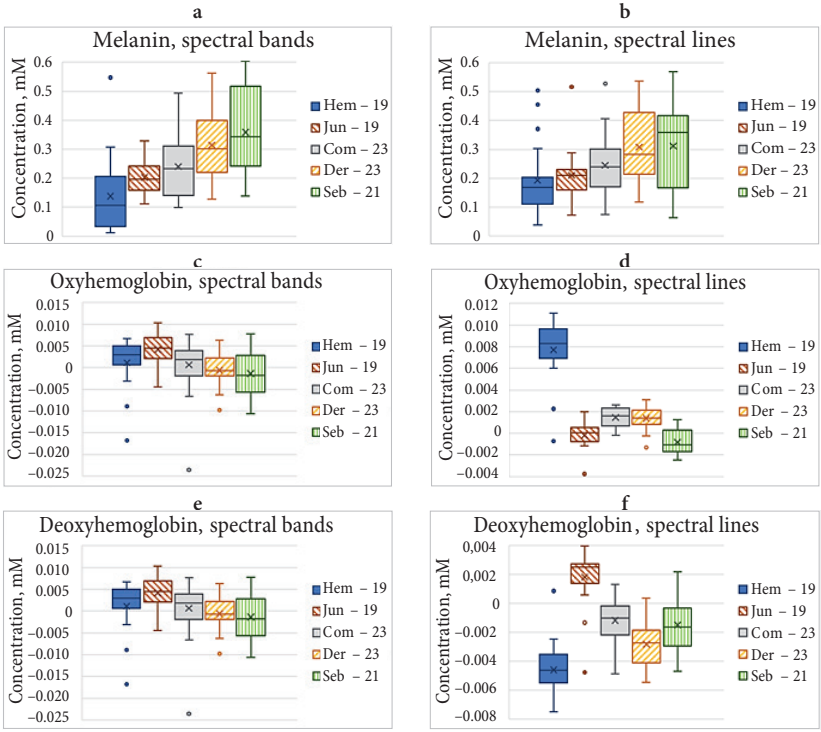

Figure 4.2 **Comparison of relative concentrations of melanin (a, b), oxyhemoglobin (c, d) and deoxyhemoglobin (e, f) in hemangiomas (*Hem*), junctional nevi (*Jun*), combined nevi (*Com*), dermal nevi (*Der*) and seborrheic keratoses (*Seb*) calculated using the spectral band device (a, c, e) and the spectral line device (b, d, f). Rectangles in graphs describe 25%–75% values, vertical lines – standard deviations, crosses – mean values, horizontal lines – median values, circles – outliers** [P2]

Figure 4.2 shows the relative concentration values of melanin, oxyhemoglobin and deoxyhemoglobin obtained from measurements using the spectral band device (Fig. 4.2 (a), (c), (e)) and the spectral line device (Fig. 4.2 (b), (d), (f)). Negative oxy- and deoxyhemoglobin values indicate that the neoplasms contain less specific chromophores than the surrounding healthy skin.

All types of neoplasms showed positive (increased) melanin values using both types of illumination. Hemangiomas show the least increase in melanin and can be well distinguished from dermal nevi.

In spectral line measurements, hemangiomas show higher oxyhemoglobin values than other neoplasms. On the other hand, seborrheic keratoses show reduced values. Junctional nevi can be distinguished from combined and dermal nevi. In spectral band measurements, relative oxyhemoglobin values overlap for all neoplasms. Junctional nevi show the highest values.

Junctional nevi can be well distinguished by graphs of relative concentrations of deoxyhemoglobin in spectral line measurements. Mostly all neoplasms show a reduced concentration of deoxyhemoglobin compared to healthy skin. In spectral band measurements, the mean deoxyhemoglobin values are much closer between different formation groups.

The results obtained using the spectral line device showed a greater potential to classify vascular neoplasms from pigmented neoplasms compared to the spectral band device.

The research presented in this subsection is published in paper P2.

4.1.2. Diagnosis of neoplasms using chromophore maps

This subsection describes the chromophore maps obtained with three, four and five laser line illumination devices.

In the first series of measurements with a three laser line illumination device, 96 different skin neoplasms were examined: 58 nevi, 23 seborrheic keratoses, 10 hemangiomas, two actinic keratoses, two *lentigo solaris,* one *macula pigmentosa.* Figure 4.3 shows two typical examples. Hemangioma shows an increased concentration of oxyhemoglobin and practically no changes in the map of melanin concentrations. On the other hand, nevi show increased melanin concentration and hemoglobin concentration values comparable to healthy skin.

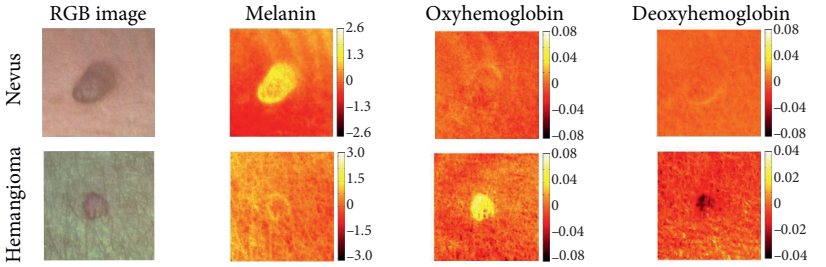

Figure 4.3 **Images of neoplasms taken with a three laser line illumination device and relative chromophore concentration maps compared to healthy skin, mM** [P7, K9]

Figure 4.4 shows the average melanin concentration values for the examined groups of neoplasms. Nevi and seborrheic keratoses show an increased concentration of melanin compared to adjacent healthy skin. In contrast, the concentration of melanin in hemangiomas and actinic keratoses does not differ significantly. *Lentigo solaris* and *macula pigmentosa* are light brown colored skin lesions with a slightly higher concentration of melanin. Both hemangiomas and actinic keratoses showed increased values of oxyhemoglobin concentration. See graphs of the distribution of average oxy- and deoxyhemoglobin concentrations in the dissertation subsection 3.1.2. Fig. 3.6 and 3.7.

In the second series of measurements, 255 different formations were examined (see subsec. 2.2.1. Tab. 2.1 in the dissertation).

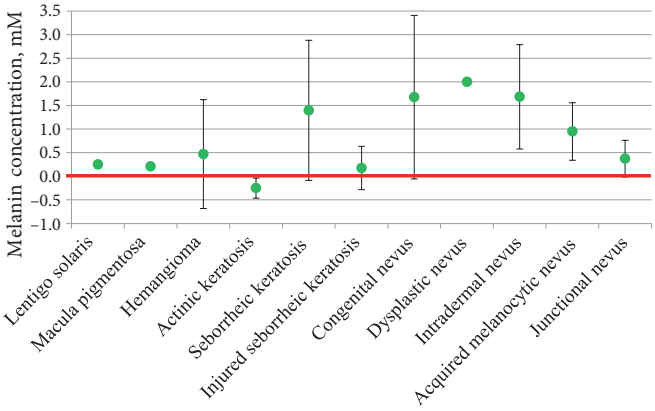

Figure 4.4 **Average melanin concentration for different skin neoplasms. The red line marks the level of healthy skin or zero** [30]

Figure 4.5 shows an example of the results for seborrheic keratosis obtained with a four laser line illumination device with one camera. A total of 117 different skin neoplasms were taken by this device (see dissertation subsec. 2.2.1. Tab. 2.1). The observed seborrheic keratosis has an increased three-dimensional structure, so it can be easily observed under 850 nm illumination. None of the four chromophore maps show considerably increased or decreased values. Seborrheic keratoses are often confused with melanomas, so autofluorescence images are used. In them, seborrheic keratoses appear as very bright formations.

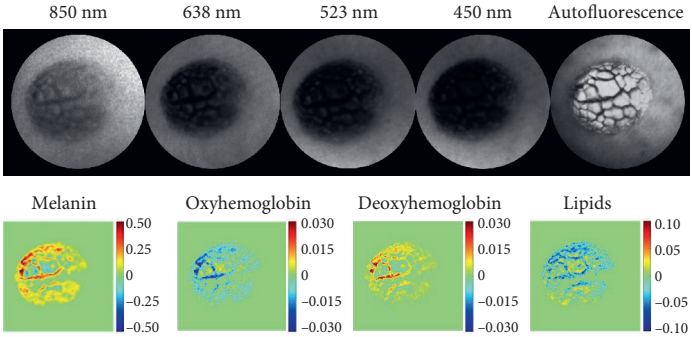

Figure 4.5 **Spectral line and autofluorescence images of seborrheic keratosis taken with a four laser line illumination device and four calculated chromophore maps. Scale values for melanin and hemoglobin are mM, lipids are M** [P6]

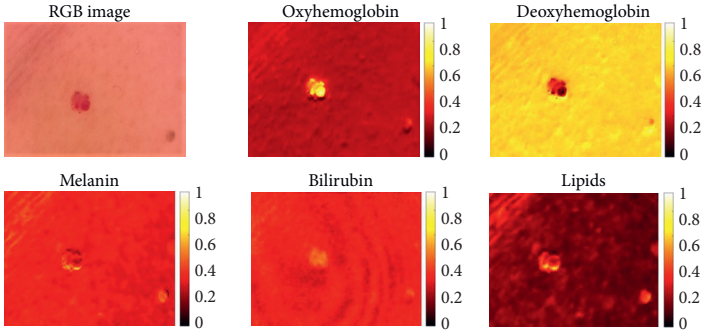

Figure 4.6 **Image of a hemangioma taken with a five laser line illumination device and relative chromophore concentration maps normalized from 0 to 1 for each image individually throughout their range of values**

33 different benign skin neoplasms: hemangiomas, nevi and seborrheic keratoses were analyzed with a five laser line illumination device. An example of chromophore maps for a hemangioma is shown in Figure 4.6. In this case, the calculated chromophores are melanin, oxy- and deoxyhemoglobin, bilirubin and lipids. Pronounced changes can be observed in the maps of oxyhemoglobin and deoxyhemoglobin – the concentration of oxyhemoglobin is much higher than in the adjacent healthy skin, while the concentration of deoxyhemoglobin is significantly lower. There are no marked changes in bilirubin and lipid maps. According to the anatomical data of the hemangioma, elevated values of bilirubin and lipid concentrations are not expected.

The research presented in this subsection is published in articles P6, P7, K5, K8, K9, and K10.

4.1.3. Diagnosis of neoplasms with the 3D-representation method

In this subsection skin neoplasms pixel analysis is reviewed from images captured using a three spectral line illumination device. 99 lesions were examined: 27 dermal nevi, 17 junctional nevi, 16 combined nevi, 22 seborrheic keratoses, 12 hemangiomas, three basal cell carcinomas, one melanoma, and one blue nevus.

Attenuation coefficients (k_i) were calculated for all neoplasms, which describe the ratio of the reflected intensities of the neoplasm and the adjacent healthy skin: k_R corresponds to 659 nm, k_G – 532 nm, k_B – 448 nm. Since the attenuation coefficients of three different wavelengths were examined, the obtained results can be represented in three-dimensional graphs (Fig. 4.7). Each point in the graphs corresponds to a pixel of the clinical measurement images of the segmented neoplasms.

Figure 4.7 (a) compares the attenuation coefficient data for three different benign neoplasms: dermal nevi, seborrheic keratoses and hemangiomas.

Although some of the clouds corresponding to the neoplasms overlap, the area occupied by the hemangioma cloud shows individual values in the graphs, so they can be distinguished from other benign neoplasms. Figure 4.7 (b) shows the data for blue nevus, melanoma and basal cell carcinoma. It can be seen that all these neoplasms can be easily distinguished – each of them occupies a certain area in the graph of the attenuation coefficient. Figure 4.7 (c) compares attenuation coefficient clouds for three different nevi: combined, dermal and junctional nevi. Although most parts of attenuation coefficient clouds overlap, each type of nevus occupies its own volume fraction in the graph. Figure 4.7 (d) compares the malignant formations – melanoma and basal cell carcinoma – with the benign dermal nevus. In this case, some values also overlap, however, k_R values for nevi are mostly higher than for melanomas and lower than for basal cell carcinomas. Each of the reviewed neoplasm groups occupies a specific volume part in the three-dimensional graphs of attenuation coefficients.

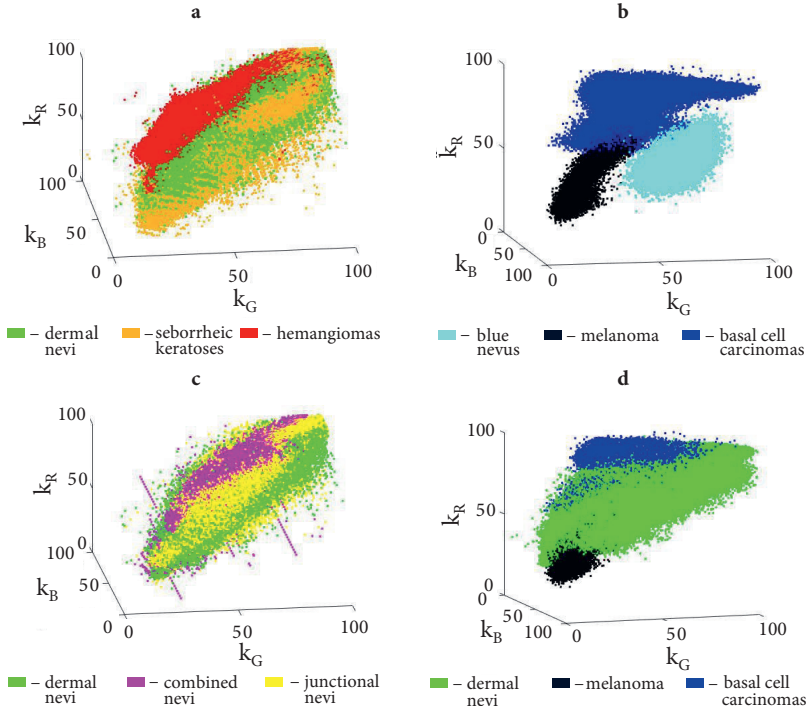

Figure 4.7 **Three-dimensional graphs of attenuation coefficients expressed as a percentage for different skin neoplasms: dermal nevi, seborrheic keratoses and hemangiomas (a), blue nevi, melanoma and basal cell carcinomas (b), dermal, combined and junctional nevi (c), dermal nevi, melanoma and basal cells carcinomas (d)** [P1]

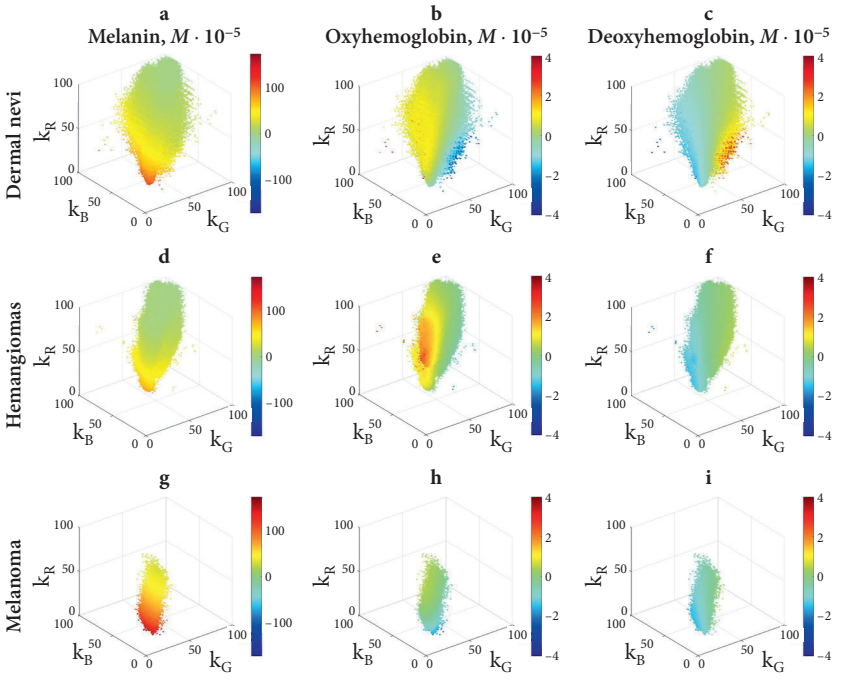

Figure 4.8 **Relative concentrations of chromophores in the 3D representation of three different types of neoplasms: dermal nevi (a-c), hemangiomas (d-f) and melanoma (g-i). The color scale indicates the increase or decrease in chromophore concentrations compared to adjacent healthy skin in moles ·10^{-5}** [P1]

The values of three chromophores in the coordinates of three attenuation coefficients were individually examined for each type of skin neoplasm. Here are examples of three different skin neoplasms: dermal nevi, hemangiomas, and melanoma (Fig. 4.8). The green color in the graphs represents the parts of neoplasms where the concentration of chromophores is the same as in the adjacent healthy skin. If the relative concentration of chromophores in the neoplasms is higher than in the skin, the data points are colored yellow to red. If the relative concentration is lower, these points are blue.

Each skin formation has a slightly different cloud of 3D values in the attenuation coefficient plots. Moreover, the distribution of chromophore values of each formation is individual. For example, dermal nevus and melanoma show the highest melanin concentration values (Fig. 4.8 (a), (g)), while hemangiomas show the highest oxyhemoglobin values (Fig. 4.8 (e)).

In summary, a new method for neoplasm analysis using three spectral line images is proposed. Clinical data were converted into 3D attenuation coefficient graphs at three wavelengths of 448 nm, 532 nm, and 659 nm. Although

the 3D data clouds partially overlap, certain characteristic features of the neoplasms can be seen both by the shape and location of the clouds in the attenuation coefficient cube and by the distribution of chromophores in them. This method shows greater potential in the classification of various neoplasms compared to the previously discussed mapping of chromophores in a two-dimensional plane. Chromophore maps provide more information about each neoplasm individually and the distribution of chromophores within it. On the other hand, the 3D representation provides greater insight into the common trends in the distribution of chromophore concentrations of different neoplasm groups. In the future, artificial intelligence could be used for such 3D cloud recognition.

The research presented in this subsection is published in paper P1.

4.2. Analysis of Beer-Lambert law models

Non-negative chromophore values in the case of the white reference

This section analyzes four Beer-Lambert law models (see subsec. 3.2.3). All possible model values in cubes of attenuation coefficients were considered: k_R corresponds to an attenuation coefficient of 659 nm, k_G – 532 nm, and k_B – 448 nm. For each point of the cube, the values of three chromophores were calculated: melanin, oxyhemoglobin and deoxyhemoglobin. Here a case is considered where the white reference is used to calculate the chromophore concentrations. In the graphs of Figure 4.9, only those points are left for which all three chromophore values are non-negative at the same time, as it should be in the case of a white reference. For each BLL model, the percentage of non-negative values in the entire cube of attenuation coefficients was calculated: for the first – 1.40 %, for the second – 0.03 %, for the third – 2.75 %, for the fourth – 1.35 %. The third model showed the largest number of valid values, so it might be the most useful for determining absolute chromophore concentrations.

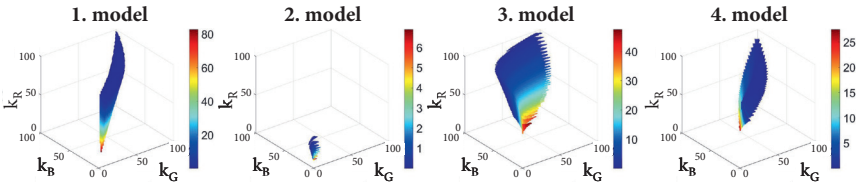

Figure 4.9 **Melanin concentration values in cubes of attenuation coefficients for the four considered BLL models, scale values moles ·10^{-5}** [K1]

Analysis of neoplasms

To study the four selected Beer-Lambert law models another approach was used – the three-dimensional representation of two groups of neoplasms was compared: hemangiomas and melanoma. The neoplasms discussed in subsection 4.1.3 were analyzed.

Figure 4.10 shows the 3D clouds of hemangiomas and melanomas with calculated oxyhemoglobin and melanin values, respectively, using the four BLL models. Hemangiomas are vascular neoplasms; therefore, the oxyhemoglobin values should be higher than the values of healthy skin. This appears to be true in the first and second models. Melanomas are pigmented neoplasms, accordingly higher values in melanin graphs would be expected. As can be seen, only the first and fourth models show elevated values. Therefore, the second and third models do not give accurate results.

Based on these data, the first model most accurately reflects the concentrations of chromophores in relation to healthy skin. The second model did not show the expected results in the case of melanoma, the third and fourth models – in the case of hemangioma and melanoma.

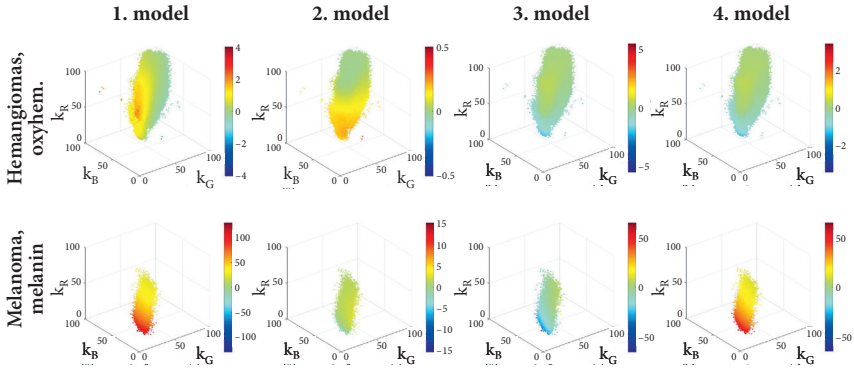

Figure 4.10 **Relative oxyhemoglobin and melanin concentrations of hemangiomas and melanoma respectively for four BLL models in 3D representation. The color scale indicates the increase or decrease in chromophore concentrations compared to the adjacent skin in moles ·10^{-5}**

The research presented in this subsection is published in the article K1.

4.3. Experiments with skin phantoms

Three kinds of skin phantoms of different thicknesses (0.9 cm, 1.5 cm and 3.3 cm) were examined (see sec. 3.3). Figure 4.11 shows the dependence of the absorption coefficient on the concentration of hemoglobin in the transmitted light measurements. As the concentration of hemoglobin increases, the absorption of light in the samples also increases linearly. The largest changes in concentration values appeared in blue light, and the smallest changes were in red light. The results obtained with a spectral band (LED) device and a three laser line illumination device were compared.

Figure 4.12 compares the average calculated hemoglobin extinction coefficient values obtained with the spectral band device and the three laser line illumination device in comparison with the values obtained by other authors [59] in diffusely reflected and transmitted light. The best resemblance of the calculated extinction coefficient values compared to other authors results appears in the diffusely reflected light measurements. The experimentally obtained results were more accurate using the spectral line device compared to the spectral band device.

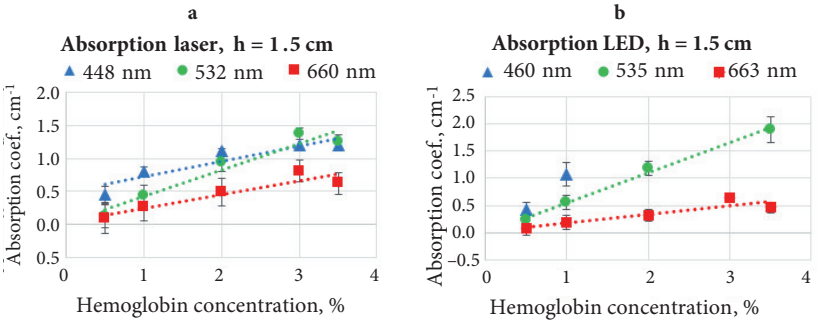

Figure 4.11 **Dependence of hemoglobin absorption coefficient on hemoglobin concentration measured by three laser line illumination device (a) and spectral band device (LED) (b) of skin phantoms** [K4]

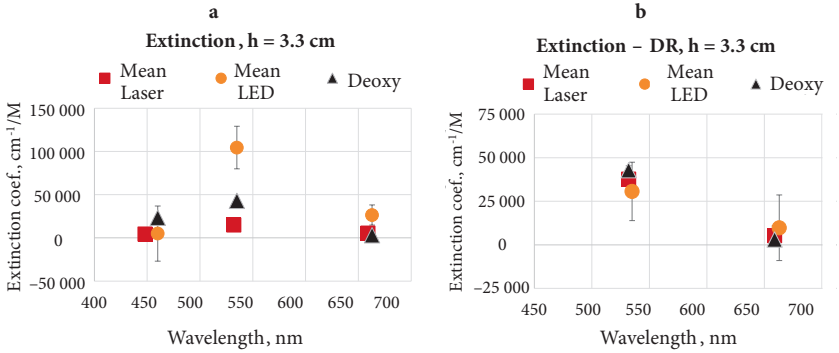

Figure 4.12 **Spectral dependence of the experimentally calculated extinction coefficients compared to the values obtained by other authors (*Deoxy*) [59]. In the case of transmitted (a) and diffusely reflected light (b)** [K4]

Skin phantoms with vascular formations were analyzed using diffusely reflected light images under red and green illumination. Hemoglobin concentration maps were calculated for the simulated blood vessels obtained from the water hemoglobin solution (Fig. 4.13). The concentration maps are slightly

different for red and green illumination. This can be explained by considering that radiation of different wavelengths penetrates to different depths and the displayed concentration values are averaged over the entire photon path length in the phantom. It should also be taken into account that the hemoglobin particles slightly diffuse to the adjacent parts of the phantom, thus reducing the final concentration.

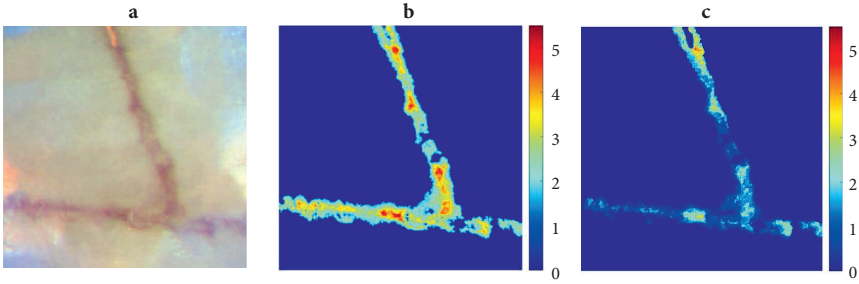

Figure 4.13 **RGB image of a two-layer blood vessel phantom (a) and calculated hemoglobin concentration maps obtained from the green (b) and red (c) spectral band device image. The scale values are μM** [K4]

In summary, it is possible to determine the concentration of chromophores and the extinction coefficient in skin phantoms both by the spectral line and by the spectral band method. However, the spectral line method provides more accurate results.

The research presented in this subsection is published in the article K4.

4.4. Signs of counterfeit money in spectral line images

4.4.1. Comparative measurements of spectral images of authentic and counterfeit banknotes

Spectral line images of 500 EUR banknotes were compared between counterfeit and authentic banknotes. 500 EUR banknotes are usually counterfeited with high quality because they are carefully inspected. In this case, also, specifically professionally counterfeited banknotes are examined. Several areas of the banknotes were analyzed to determine the most difficult to forge parts under spectral line illumination (Fig. 4.14).

Figure 4.14 **500 EUR banknote from the front (a) and back (b) with regions of interest outlined**

The signature and stars are visible in the first selected area (Fig. 4.15). Visually, the stars look the same on both banknotes, but under 659 nm illumination, the star on the right side of the authentic banknote absorbs less light than the background around it, while the star on the counterfeit appears darker. In this case, it would be useful to create a program that recognizes the shape of the star and calculates its average value against the surrounding background.

Buildings of modernist architecture under number "5" were examined in the second selected area of the front side of the 500 EUR banknote (Fig. 4.15). In the counterfeit banknote, several parallel stripes on the building are visible, which are not visible in the authentic banknote. These stripes may be caused by the printer used for forgery. Such or similar defects caused by printers could easily be identified as inappropriate design elements. In the third area, it can be seen that on the yellow rectangle in the lower left corner of the back of the banknote, the words "EURO" and "EYPΩ" are well distinguished for an authentic banknote, but in the case of a counterfeit, the words blend into the background.

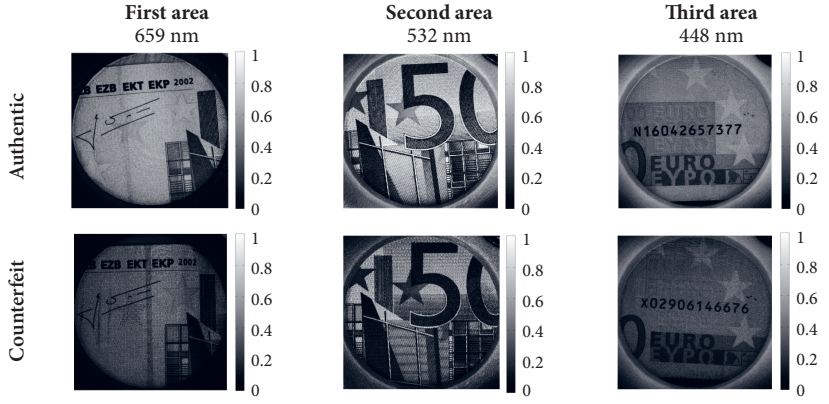

Figure 4.15 **Spectral line images of an authentic and counterfeit 500 EUR banknote in three selected areas of interest**

20 EUR banknotes are the most frequently counterfeited because usually, people do not pay as much attention to them. For this reason, counterfeits are usually of poor quality. Many counterfeits can be detected by a closer look at the banknote. Areas of the 20 EUR banknote where the spectral line images were compared between authentic and counterfeit banknotes are shown in Figure 4.16 (a).

The spectral line image ratios were examined. Some of the results are shown in Figure 4.17. In the ratios of spectral images in the first area difference between the authentic banknote and counterfeits in the mottled background on the right can be seen. A fine concrete structure can be seen in an authentic banknote, while in a counterfeit it is not pronounced. In the second area, a star can be seen in the number "2" in the counterfeit example, but not in the authentic banknote. In the third area distinct white dots are visible in the image window, which do not appear at all in the counterfeit.

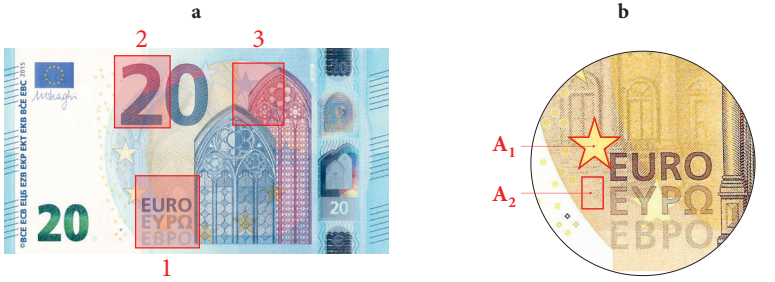

Figure 4.16 **20 EUR new style banknote from the front with highlighted regions of interest (a) and elements used for numerical analysis on the front side of the 50 EUR banknote (b)** [K7]

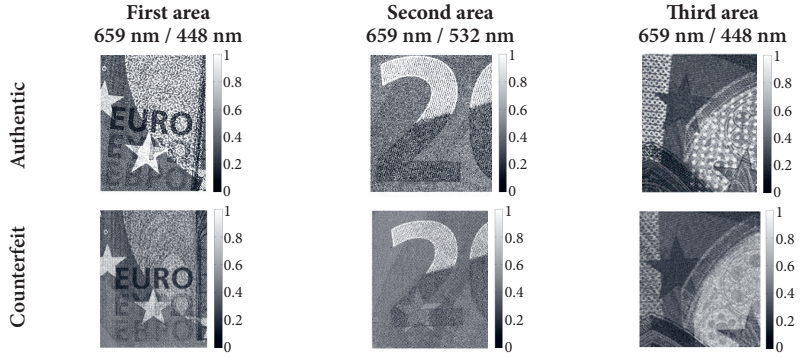

Figure 4.17 **Spectral line image ratios of authentic and counterfeit 20 EUR banknote** [K8]

The research presented in this subsection is published in the article K8.

4.4.2. Comparative measurements of spectral image values of authentic and counterfeit banknotes

For the 50 EUR banknote, the numerical results of two element pairs were compared for counterfeits and authentic banknotes. The intensity of the star (A_1) was compared with the background (A_2) around it (Fig. 4.16 (b)). Both monochromatic values (λR, λG and λB) and spectral line image ratios and differences were compared. The obtained results are shown in Figure 4.18.

Authentic banknotes, counterfeits created using an inkjet printer (Counterfeit 1) and other types of counterfeits (Counterfeit 2) were analyzed (Fig. 4.18). According to the obtained results, spectral divisions in red and blue illumination (λR/λB), as well as in green and blue illumination (λG/λB) for authentic banknotes show certain trends – their numerical values are much higher than for counterfeits.

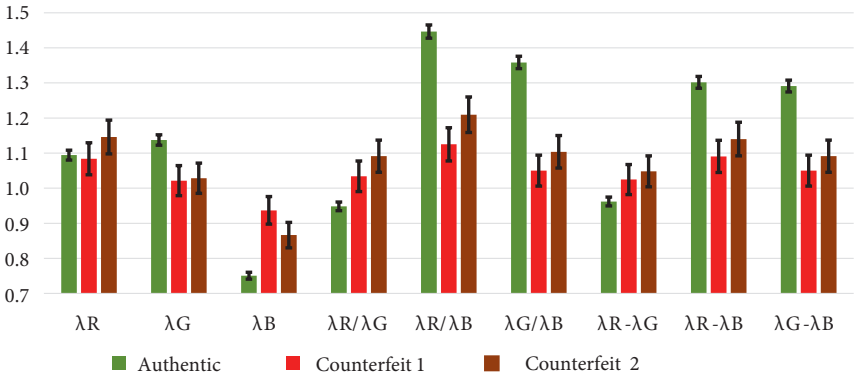

Figure 4.18 **Intensity ratios between elements A_1 and A_2 for images of spectral lines (λR, λG and λB), their divisions and differences** [K7, K8]

When these results and the visual evaluations described above are taken into account, we can conclude that images of spectral lines and their various relationships provide information that is essential in the recognition of counterfeit banknotes.

The research presented in this subsection is published in articles K7 and K8.

4.5. Detection of forged documents

Each of the three pages of the sample document was individually examined using a three laser line illumination device. Average values for printed texts were calculated (Tab. 4.1). According to the obtained results, the calculated average color toner values for the first and third pages are very close, but for the second

page, they are significantly different. This could indicate that a different printer or ink cartridge was used to print the second page.

Handwritten signatures were similarly analyzed to verify that the same ink pens were used on all pages. The results of the first signature are summarized in Table 4.2. From this analysis, it is not possible to determine whether the inks used for the signatures were different or the same on all pages, as the results may vary depending on how hard the writer presses the pen on the paper, the type of paper used, and other conditions.

Table 4.1 **Spectral line images obtained with a three laser line illumination device and calculated average values for printed texts for three document pages** [P3]

Nr.	659 nm	Av. value, $\cdot 100^{-1}$	532 nm	Av. value, $\cdot 100^{-1}$	448 nm	Av. value, $\cdot 100^{-1}$
1	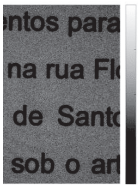	2.9 ± 1.5	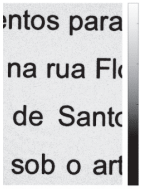	7.8 ± 3.5	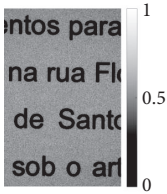	5.1 ± 0.4
2		4.2 ± 1.7	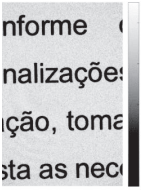	9.8 ± 3.6	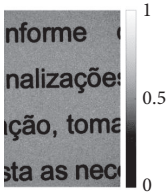	6.3 ± 0.4
3		2.8 ± 1.5	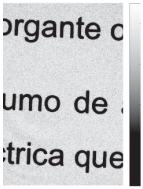	7.3 ± 3.3	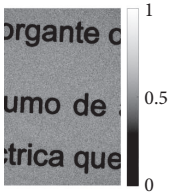	5.1 ± 0.4

Table 4.2 **Average values of the first signature in all spectral line images and their ratios in three document pages.**

Page No.	659 nm	532 nm	448 nm	448 nm / 532 nm	659 nm / 448 nm	532 nm / 659 nm
1	0.080 ± 0.026	0.253 ± 0.058	0.303 ± 0.046	1.80 ± 0.21	0.42 ± 0.09	1.34 ± 0.23
2	0.088 ± 0.037	0.289 ± 0.095	0.313 ± 0.062	1.71 ± 0.36	0.44 ± 0.12	1.36 ± 0.23
3	0.060 ± 0.022	0.189 ± 0.048	0.252 ± 0.041	2.00 ± 0.23	0.38 ± 0.10	1.34 ± 0.25

Using the method discussed here for document forgery detection, it was possible to recognize a different type of toner for printed texts, while potential signature forgeries with similar ink could not be detected. Although the method only partially worked for this research purpose, it did not damage the sample, so it would work well with destructive methods as an additional information provider.

The research presented in this subsection is published in paper P3.

SUMMARY

This work discusses the spectral line imaging method and two potential applications of it. The method is non-invasive, spectrally sensitive, fast and easy to use. Compared to multispectral and hyperspectral imaging, higher quality images are obtained – without motion artifacts, because the data is acquired with only one or two snapshots. The amount of data is significantly reduced, so data processing is easier and faster.

Several test devices were created for experimental measurements with this method, including three-line, five-line and two four-line illumination devices. With a three laser line illumination device (448 nm, 532 nm, and 659 nm), only one color image is captured, which is later split into three spectral images at each of the illumination wavelengths using an RGB crosstalk correction algorithm. In a five laser line illumination device (405 nm, 450 nm, 525 nm, 656 nm, and 850 nm), two images are captured under the illumination of three and two laser lines. The latest development is four laser line illumination devices (450 nm, 523 nm, 638 nm, and 850 nm) with two or one camera for imaging. The laser beams are focused into an optical fiber loop that provides uniform illumination of the object. With all these devices it is possible to take high-quality spectral line images.

Using the created spectral line imaging devices, clinical measurements were performed on skin neoplasms under the supervision of a qualified dermatologist, in accordance with ethical approval. Both benign and malignant neoplasms (nevi, hemangiomas, melanomas, basal cell carcinomas, etc.) were examined. The relative concentration values of skin chromophores in relation to healthy skin were calculated using a modified Beer-Lambert law and attenuation coefficients at the specific wavelengths. The obtained results corresponded well to anatomically expected – hemangiomas (vascular neoplasms) showed increased oxyhemoglobin values, while nevi (pigmented neoplasms) showed increased melanin values. The concentration of lipids in neoplasms was also examined with the device of four laser lines, and the concentration of both lipids and bilirubin – with the device of five laser lines.

A new three-dimensional data analysis approach using spectral attenuation values for three wavelengths is proposed for obtaining a more general idea of the distribution of chromophore concentration changes in various neoplasms. All pixel values of the segmented neoplasm images were included in the 3D graphs, therefore creating three-dimensional data point clouds corresponding to each neoplasm group. For different skin neoplasms, the pixel clouds form individually specific shapes and occupy different spatial positions. Using this data and the distribution of chromophore concentrations, it is possible to clearly distinguish different groups of neoplasms.

In addition, a spectral band illumination device with spectral peaks at 460 nm, 535 nm, and 663 nm was used. Average values and maps of chromophore

concentrations obtained and calculated with the spectral band and spectral line illumination devices were compared for different groups of neoplasms. Chromophore maps showed more anatomically relevant values in spectral line images compared to the spectral band images. Statistical data also confirmed the better potential for the classification of neoplasms in the case of the spectral line device.

To find the best method for detecting changes in chromophore concentrations in skin neoplasms, four different models of a modified Beer-Lambert law were tested. The first model examines the absorption of three main skin chromophores; the second model takes into account the absorption due to other chromophores and the penetration depth of different wavelengths into the skin; the third model uses the effective attenuation coefficient instead of the absorption coefficient, which also includes scattering; the fourth model considers the skin as a five layered structure. The models were analyzed using 3D graphs of attenuation coefficients. When analyzing *in vivo* measurements of neoplasms by using adjacent healthy skin as a reference the best results were achieved using the first model.

To test the accuracy of the spectral line imaging method, several skin phantoms were created from agar, intralipid and hemoglobin powder at different concentrations. Measurements were taken with the three laser line illumination device and the three spectral band illumination device for both transmitted and diffusely reflected light. The spectral line device data showed more repeatable extinction coefficient values than the spectral band device data, and these values corresponded well with the deoxyhemoglobin extinction coefficient values found in the literature. It was concluded that measurements of spectral line images provide better quality data than measurements of spectral band images.

In cooperation with the Bank of Latvia, measurements of spectral line images were taken from authentic and counterfeit EUR banknotes, which were removed from circulation. 20 EUR, 50 EUR and 500 EUR banknotes were analyzed. It was concluded that even in the case of professional counterfeits, there are differences in the spectral line images from those of authentic banknotes, even though the colors do not differ visually. In the spectral line image ratios, structures appeared in the authentic 20 EUR banknotes which are not observable in white light and do not appear in counterfeits either. A pair of elements on a 50 EUR banknote was chosen for numerical comparison: a star with its background. Using the spectral ratios of these or other elements in the images, it is possible to confidently distinguish counterfeits from authentic banknotes.

A potentially suspicious document prepared in the forensic laboratory of the Portuguese police, consisting of three pages printed on one side with three signatures on each page was analyzed. The results of measurements made with a three spectral line illumination device revealed that the printed text on the first and third page is not spectrally different, while a different printer was most likely used to print the text on the second page. Analyzing the signatures on

the printed pages – both the average values of the signatures of the spectral lines and their ratios – different average values were obtained, however, they did not differ within the error interval.

MAIN RESULTS AND CONCLUSIONS

- Prototypes for obtaining images of three, four and five spectral lines at wavelength combinations 450/532/659 nm, 450/523/638/850 nm and 405/450/525/656/ 850 nm have been created and laboratory/clinically approved. Programs for spectral line image processing were created in a *Matlab* environment and tested. [P1, P2, P3, P5, P6, P7, P8, K2, K3, K4, K5, K6, K7, K8, K9, K10, K11, R1, R2, R4]
- Clinical data on dermal nevi, junctional nevi, combined nevi, blue nevi, hemangiomas, seborrheic keratoses, basal cell carcinomas and melanomas have been obtained using the multi-spectral line snapshot imaging method. A new non-contact diagnostic method is proposed using attenuation coefficients of diffuse reflection intensity at three wavelengths in 3D representation. The study of four modifications of the Beer-Lambert law was carried out and the most suitable model for the calculations of spectral line images into distribution maps of the three main skin chromophores (melanin, oxyhemoglobin and deoxyhemoglobin) was proposed. [P1, P2, P4, P6, P7, P8, K1, K4, K5, K8, K9, K10, K11, R1, R4]
- The method of spectral line imaging was compared with the method of spectral band imaging by using skin phantoms and *in vivo* measurements of neoplasms as samples. It was concluded that the spectral line imaging method provides more accurate values and is more useful for the classification of neoplasms. [P2, K4]
- Comparative measurements of twenty-nine 20 EUR banknotes, twenty-nine 50 EUR banknotes and six 500 EUR banknotes, as well as three samples of document pages for the detection of forgeries, were performed using the spectral line imaging method. In all cases, specific variations in the images of spectral lines, their divisions and differences were found, and a new algorithm for recognizing counterfeit money was proposed. Pen ink recognition with this method did not provide the desired accuracy. [P3, K7, K8, R1, R3]

BIBLIOGRAPHY

[1] Ifa, D.R. *et al.* (2007) Development of capabilities for imaging mass spectrometry under ambient conditions with desorption electrospray ionization (DESI). *Int. J. Mass Spectrom.* 259, 8–15

[2] Kula, A. *et al.* (2014) Application of laser induced breakdown spectroscopy to examination of writing inks for forensic purposes. *Sci. Justice* 54, 118–125

[3] Dhara, S. *et al.* (2010) Forensic application of total reflection X-ray fluorescence spectrometry for elemental characterization of ink samples. *Spectrochim. Acta - Part B At. Spectrosc.* 65, 167–170

[4] Waddell, A. *et al.* (2018) Advances in the use of reflectance confocal microscopy in melanoma. *Melanoma Manag.* 5, MMT04

[5] Mogensen, M. *et al.* (2009) Optical Coherence Tomography for Imaging of Skin and Skin Diseases. *Semin. Cutan. Med. Surg.* 28, 196–202

[6] Udriştioiu, F.M. *et al.* (2012) Application of Micro-Raman and FT - IR Spectroscopy in Forensic Analysis of Questioned Documents. *Gazi Univ. J. Sci.* 25, 371–375

[7] Saiko, G. *et al.* (2020) Hyperspectral imaging in wound care: A systematic review. *Int. Wound J.* 17, 1840–1856

[8] Aloupogianni, E. *et al.* (2022) Hyperspectral and multispectral image processing for gross-level tumor detection in skin lesions: a systematic review. *J. Biomed. Opt.* 27, 1–28

[9] Spigulis, J. (2014) Method for imaging of spectral reflectance at several wavelengths, WO2015071786A1

[10] Spigulis, J. and Elste, L. (2012) Method and device for imaging of spectral reflectance at several wavelength bands, WO2013135311 (A1)

[11] Cui, R. *et al.* (2022) Deep Learning in Medical Hyperspectral Images: A Review. *Sensors* 22

[12] Lu, G. *et al.* (2015) Framework for hyperspectral image processing and quantification for cancer detection during animal tumor surgery. *J. Biomed. Opt.* 20, 126012

[13] Demir, B. and Ertürk, S. (2008) Empirical mode decomposition pre-process for higher accuracy hyperspectral image classification. *Int. Geosci. Remote Sens. Symp.* 2

[14] Fei, B. *et al.* (2017) Label-Free Hyperspectral Imaging and Quantification Methods for Surgical Margin Assessment of Tissue Specimens of Cancer Patients. *Annu Int Conf IEEE Eng Med Biol Soc.* PMC6169991, 4041–4045

[15] Kong, S.G. *et al.* (2005) Hyperspectral fluorescence image analysis for use in medical diagnostics. *Adv. Biomed. Clin. Diagnostic Syst. III* 5692, 21

[16] Mou, L. *et al.* (2022) Deep Reinforcement Learning for Band Selection in Hyperspectral Image Classification. *IEEE Trans. Geosci. Remote Sens.* 60, 1–14

[17] Sun, W. and Du, Q. (2019) Hyperspectral band selection: A review. *IEEE Geosci. Remote Sens. Mag.* 7, 118–139

[18] Tan, K. *et al.* (2014) Hyperspectral image classification using band selection and morphological profiles. *IEEE J. Sel. Top. Appl. Earth Obs. Remote Sens.* 7, 40–48

[19] Yu, H. and Yang, J. (2001) A direct LDA algorithm for high-dimensional data – with application to face recognition. *Pattern Recognit.* 34, 2067–2070

[20] Lu, G. *et al.* (2016) Hyperspectral Imaging of Neoplastic Progression in a Mouse Model of Oral Carcinogenesis. *Med. Imaging 2016 Biomed. Appl. Mol. Struct. Funct. Imaging* 34, 206–213.

[21] Madooei, A. *et al.* (2017) Hyperspectral image processing for detection and grading of skin erythema. *Med. Imaging 2017 Image Process.* 10133, 1013322

[22] Wambugu, N. *et al.* (2021) Hyperspectral image classification on insufficient-sample and feature learning using deep neural networks: A review. *Int. J. Appl. Earth Obs. Geoinf.* 105, 102603

[23] Hu, B. *et al.* (2019) Tumor tissue classification based on micro-hyperspectral technology and deep learning. *Biomed. Opt. Express* 10, 6370

[24] Aboras, M. *et al.* (2015) Early detection of melanoma using multispectral imaging and artificial intelligence techniques. *Am. J. Biomed. Life Sci.* 3, 29–33

[25] Gao, L. and Smith, R.T. (2015) Optical hyperspectral imaging in microscopy and spectroscopy – a review of data acquisition. *J. Biophotonics* 8, 441–456

[26] Spigulis, J. and Elste, L. (2014) Single snapshot RGB multispectral imaging at fixed wavelengths: proof of concept. *Proc. SPIE 8937, Multimodal Biomed. Imaging IX*

[27] Spīgulis, J. and Ošiņa, I. (2022) Spectral line imaging: principles, implementation and applications. *Latv. Acad. Sci. Yearb.*

[28] Le, H.Q. and Wang, Y. (2010) Semiconductor laser multi-spectral sensing and imaging. *Sensors* 10, 544–583

[29] Jakovels, D. and Spigulis, J. (2010) Skin haemoglobin mapping: comparison of multi-spectral imaging and selective R-G-B analysis. *Biomed. Opt. 3-D Imaging, OSA Tech. Dig. (Optica Publ. Group, 2010)*

[30] Ošiņa, I. (2017) Ādas hromoforu kartēšana 3,4 un 5 spektrālo līniju apgaismojumā. *Univ. Latv.,* Master thesis.

[31] Kviesis-Kipge, E. (2019) Development of skin chromophore mapping device using five spectral line illumination. *Opt. InfoBase Conf. Pap.* Part F157-, 3–4

[32] So, P.-L. (2007) *Skin Cancer (The Biology of Cancer)*, Chelsea House Pub

[33] Igarashi, T. *et al.* (2007) The appearance of human skin: A survey. *Found. Trends Comput. Graph. Vis.* 3, 1–95

[34] Anderson, R.R. and Parrish, J.A. (1981) The optics of human skin. *J. Invest. Dermatol.* 77, 13–19

[35] Habif, T.P. (2015) *Clinical Dermatology A Color Guide to Diagnosis and Therapy*, (Sixth.), Saunders

[36] Soyer, H.P. *et al.* (2001) Dermoscopy of pigmented skin lesions (Part II). *Eur. J. Dermatology* 11, 483–498

[37] Johr, R.H. and Stolz, W. (2010) *Dermoscopy: An Illustrated Self-Assessment Guide*, McGraw-Hill Education / Medical

[38] Shiga, T. *et al.* (2012) Blue nevus with a starburst pattern on dermoscopy. *Dermatol. Pract. Concept.* 2, 31–33

[39] Bowling, J. (2012) *Diagnostic Dermoscopy*, Wiley-Blackwell

[40] Nielsen, K.P. *et al.* (2008) The optics of human skin: Aspects important for human health. *Sol. Radiat. Hum. Heal.*

[41] Lister, T. *et al.* (2012) Optical properties of human skin. *J. Biomed. Opt.* 17, 0909011

[42] Parrish, J.A. *et al.* (1983) Selective Thermal Effects with Pulsed Irradiation from Lasers : From Organ to Organelle. *J. Invest. Dermatol.*

[43] Äggblad, E. (2008) In Vivo Diffuse Reflectance Spectroscopy of Human Tissue. Linköping University

[44] Lambert, J.H. (1760) *Photometria sive de mensura et gradibus luminis, colorum et umbrae*, Klett, Augustae Vindelicorum

[45] Beer, A. (1852) Bestimmung der Absorption des rothen Lichts in farbigen Flüssigkeiten. *Ann. Phys.* 162, 78–88

[46] Contini, D. *et al.* (1997) Photon migration through a turbid slab described by a model based on diffusion approximation I Theory. *Appl. Opt.* 36, 4587

[47] Hiraoka, M. *et al.* (1993) A Monte Carlo investigation of optical pathlength in inhomogeneous tissue and its application to near-infrared spectroscopy. *Phys. Med. Biol.* 38, 1859–1876

[48] Prahl, S.A. (1989) A Monte Carlo model of light propagation in tissue. *Dosim. Laser Radiat. Med. Biol.* 10305, 1030509

[49] Karamavuş, Y. and Özkan, M. (2019) Newborn jaundice determination by reflectance spectroscopy using multiple polynomial regression, neural network, and support vector regression. *Biomed. Signal Process. Control* 51, 253–263

[50] Anderson, N.M. and Paul Sekelj (1967) Light-absorbing and scattering properties of nonhaemolysed blood. *Phys. Med. Biol.* 12, 173–184

[51] Huong, A. and Ngu, X. (2014) The application of extended Modified Lambert Beer model for measurement of blood carboxyhemoglobin and oxyhemoglobin saturation. *J. Innov. Opt. Health Sci.* 7, 1–7

[52] Izzetoglu, M. and Holtzer, R. (2020) Effects of Processing Methods on fNIRS Signals Assessed during Active Walking Tasks in Older Adults. *IEEE Trans. Neural Syst. Rehabil. Eng.* 28, 699–709

[53] Ong, P.E. *et al.* (2019) Modified lambert beer for bilirubin concentration and blood oxygen saturation prediction. *Int. J. Adv. Intell. Informatics* 5, 113–122

[54] Välisuo, P. *et al.* (2011) New closed-form approximation for skin chromophore mapping. *J. Biomed. Opt.* 16

[55] Commoner, B. and Lipkin, D. (1949) The application of the Beer-Lambert law to optically anisotropic systems. *Science,* 110, 41–43

[56] Twersky, V. (1962) Multiple scattering of waves and optical phenomena. *J Opt Soc Am* 52, 145–71

[57] Delpy, D.T. *et al.* (1988) Estimation of optical pathlength through tissue from direct time of flight measurement. *Phys. Med. Biol.* 33, 1433–1442

[58] Niemz, M.H. (2007) *Laser-Tissue Interactions. Fundamentals and Applications*, (Third, Enl.), Springer

[59] Scott Prahl (1998) Tabulated Molar Extinction Coefficient for Hemoglobin in Water. *Oregon Medical Laser Center.* [Online]. Available: https://omlc.org/spectra/hemoglobin/summary.html. [Accessed: 02-Nov-2022]

[60] Sarna, T. and Swartz, H. (1988) Extinction coefficient of melanin. *Oregon Medical Laser Center.* [Online]. Available: https://omlc.org/spectra/melanin/eumelanin.html. [Accessed: 02-Nov-2022]

[61] Prahl, S. (2017) Optical absorption spectrum of Bilirubin in chloroform. *Oregon Medical Laser Center.* [Online]. Available: https://omlc.org/spectra/PhotochemCAD/data/119-abs.txt. [Accessed: 02-Nov-2022]

[62] Prahl, S. (2017) Optical absorption spectrum of Beta-carotene in hexane. *Oregon Medical Laser Center.* [Online]. Available: https://omlc.org/spectra/PhotochemCAD/data/041-abs.txt. [Accessed: 02-Nov-2022]

[63] Lukinsone, V. *et al.* (2020) Remitted photon path lengths in human skin: in-vivo measurement data. *Biomed. Opt. Express* 11, 2866–2873

[64] Ferlay, J. *et al.* (2013) Cancer incidence and mortality patterns in Europe: Estimates for 40 countries in 2012. *Eur. J. Cancer* 49, 1374–1403

[65] Goodson, A.G. and Grossman, D. (2009) Strategies for early melanoma detection: approaches to the patient with nevi. *J. Am. Acad. Dermatol.* 60, 719–738

[66] Rey-Barroso, L. *et al.* (2021) Optical technologies for the improvement of skin cancer diagnosis: A review. *Sensors (Switzerland)* 21, 1–31

[67] Ahlgrimm-Siess, V. *et al.* (2011) Confocal Microscopy in Skin Cancer. *Cancer Ski.*

[68] Humbert, P.G. *et al.* (2003) Topical ascorbic acid on photoaged skin. Clinical, topographical and ultrastructural evaluation: Double-blind study vs. placebo. *Exp. Dermatol.* 12, 237–244

[69] Tchvialeva, L. *et al.* (2009) Optical discrimination of surface reflection from volume backscattering in speckle contrast for skin roughness measurements. *Photonic Ther. Diagnostics V* 7161, 71610I

[70] Ferrante di Ruffano, L. *et al.* (2018) Optical coherence tomography for diagnosing skin cancer in adults. *Cochrane Database Syst. Rev.* 2018

[71] Perchoux, J. *et al.* (2016) Current developments on optical feedback interferometry as an all-optical sensor for biomedical applications. *Sensors (Switzerland)* 16, 1–26

[72] Rakić, A.D. *et al.* (2014) THz QCL self-mixing interferometry for biomedical applications. *Terahertz Emit. Receiv. Appl. V* 9199, 91990M

[73] Spandana, K.U. *et al.* (2019) Polarization-resolved Stokes-Mueller imaging: a review of technology and applications. *Lasers Med. Sci.* 34, 1283–1293

[74] Rey-Barroso, L. *et al.* (2019) Polarized multispectral imaging for the diagnosis of skin cancer. *Final Progr. Proc. - IS T/SID Color Imaging Conf.* 2019-Octob, 381–385

[75] Louie, D.C. *et al.* (2018) Degree of optical polarization as a tool for detecting melanoma: proof of principle. *J. Biomed. Opt.* 23, 1

[76] Mazumder, N. and Kao, F.J. (2021) Stokes polarimetry-based second harmonic generation microscopy for collagen and skeletal muscle fiber characterization. *Lasers Med. Sci.* 36, 1161–1167

[77] Ghassemi, P. *et al.* (2012) Out-of-plane Stokes imaging polarimeter for early skin cancer diagnosis. *J. Biomed. Opt.* 17, 0760141

[78] Magalhaes, C. *et al.* (2019) The role of AI classifiers in skin cancer images. *Ski. Res. Technol.* 25, 750–757

[79] Li, L. *et al.* (2014) Automatic diagnosis of melanoma using machine learning methods on a spectroscopic system. *BMC Med. Imaging* 14, 1–12

[80] Marvdashti, T. *et al.* (2016) Classification of basal cell carcinoma in human skin using machine learning and quantitative features captured by polarization sensitive optical coherence tomography. *Biomed. Opt. Express* 7, 3721

[81] Rey-Barroso, L. *et al.* (2019) Morphological study of skin cancer lesions through a 3D scanner based on fringe projection and machine learning. *Biomed. Opt. Express* 10, 3404

[82] Li, Y. and Shen, L. (2018) Skin lesion analysis towards melanoma detection using deep learning network. *Sensors (Switzerland)* 18, 1–16

[83] Gautam, D. *et al.* (2018) Machine learning–based diagnosis of melanoma using macro images. *Int. j. numer. method. biomed. eng.* 34

[84] Dreiseitl, S. *et al.* (2001) A comparison of machine learning methods for the diagnosis of pigmented skin lesions. *J. Biomed. Inform.* 34, 28–36

[85] J, B.J. and Roslin, S.E. (2020) Classification of melanoma from Dermoscopic data using machine learning techniques. *Multimed Tools Appl* 79, 3713–3728

[86] Maiti, A. and Chatterjee, B. (2020) Improving detection of Melanoma and Naevus with deep neural networks. *Multimed. Tools Appl.* 79, 15635–15654

[87] Wood, A. *et al.* (2008) Evaluation of the MoleMate™ training program for assessment of suspicious pigmented lesions in primary care. *Inform. Prim. Care* 16, 41–50

[88] Menzies, S.W. *et al.* (2001) Short-term digital surface microscopic monitoring of atypical or changing melanocytic lesions. *Arch. Dermatol.* 137, 1583–1589

[89] Menzies, S.W. *et al.* (2005) The Performance of SolarScan: An Automated Dermoscopy Image Analysis Instrument for the Diagnosis of Primary Melanoma. *Arch. Dermatol.* 141, 1388–96

[90] MacLellan, A.N. *et al.* (2021) The use of noninvasive imaging techniques in the diagnosis of melanoma: a prospective diagnostic accuracy study. *J. Am. Acad. Dermatol.* 85, 353–359

[91] Phillips, J. *et al.* (2020) Dermal thickness and echogenicity using DermaScan C high frequency ultrasound: Methodology and reliability testing in people with and without primary lymphoedema. *Ski. Res. Technol.* 26, 813–823

[92] Pogue, B.W. and Patterson, M.S. (2006) Review of tissue simulating phantoms for optical spectroscopy, imaging and dosimetry. *J. Biomed. Opt.* 11, 041102

[93] Dabrowska, A.K. *et al.* (2016) Materials used to simulate physical properties of human skin. *Ski. Res. Technol.* 22, 3–14

[94] Aranda-Lara, L. *et al.* (2014) Biological Tissue Modeling with Agar Gel Phantom for Radiation Dosimetry of 99m Tc. *Open J. Radiol.* 04, 44–52

[95] van Staveren, H.J. *et al.* (1991) Light scattering in lntralipid-10% in the wavelength range of 400–1100 nm. *Appl. Opt.* 30, 4507

[96] (2022) Euro banknote counterfeiting at historically low level in 2021. *European Bank Central*. [Online]. Available: https://www.ecb.europa.eu/press/pr/date/2022/html/ecb.pr220128~d65c3326c2.en.html. [Accessed: 19-Dec-2022]

[97] Aleksandrs Antiņš (2023) Latvijā pērn konstatēts par 26,5% vairāk viltotu naudaszīmju. *LETA*. [Online]. Available: https://leta.lv/home/important/D5A2950E-2C02-447D-A074-554C615EF429/. [Accessed: 03-Apr-2023]

[98] (2019) 500 eiro banknote vairs netiks izlaista. *Latvijas Banka*. [Online]. Available: https://www.bank.lv/component/content/article?id=11682:500-eiro-banknote-vairs-netiks-izlaista. [Accessed: 19-Dec-2022]

[99] Tauriņš, A. (2020) Naudas drošība un pretviltošana. *Latvijas Banka*. [Online]. Available: https://www.bank.lv/banknotes-un-monetas/eiro-drosiba. [Accessed: 21-Nov-2022]

[100] Banka, E.C. (2022) Dizaina elementi. *Eiropas centrālā banka / Eurosistēma*. [Online]. Available: https://www.ecb.europa.eu/euro/banknotes/design/html/index.lv.html. [Accessed: 08-Dec-2022]

[101] Bruna, A. *et al.* (2013) Forgery detection and value identification of Euro banknotes. *Sensors (Switzerland)* 13, 2515–2529

[102] Lee, J.W. *et al.* (2017) A survey on banknote recognition methods by various sensors. *Sensors (Switzerland)* 17

[103] Viraktamath, S. V. *et al.* (2021) Review on detection of fake currency using image processing techniques. *Proc. - 5th Int. Conf. Intell. Comput. Control Syst. ICICCS 2021*

[104] Agarwal, A. *et al.* (2016) Review: Techniques for the Characterization of Inks. *IOSR J. Appl. Chem.* 9, 76–96

[105] Li, B. (2016) An Examination of the Sequence of Intersecting Lines using Microspectrophotometry. *J. Forensic Sci.* 61, 809–814

[106] Menzyk, A. *et al.* (2015) Physicochemical analysis of inks and methods of evidence evaluation - A review. *Z Zagadnien Nauk Sadowych* 104, 245–278

[107] Moore, K.L. *et al.* (2019) Determination of Deposition Order of Toners, Inkjet Inks, and Blue Ballpoint Pen Combining MeV-Secondary Ion Mass Spectrometry and Particle Induced X-ray Emission. *Anal. Chem.* 91, 12997–13005

[108] Calcerrada, M. and García-Ruiz, C. (2015) Analysis of questioned documents: A review. *Anal. Chim. Acta* 853, 143–166

[109] Sauzier, G. *et al.* (2015) In situ studies into the characterisation and degradation of blue ballpoint inks by diffuse reflectance visible spectroscopy. *Anal. Methods* 7, 4892–4900

[110] Neumann, C. *et al.* (2011) Forensic examination of ink by high-performance thin layer chromatography-The United States Secret Service Digital Ink Library. *J. Chromatogr. A* 1218, 2793–2811

[111] Djozan, D. *et al.* (2008) Forensic discrimination of blue ballpoint pen inks based on thin layer chromatography and image analysis. *Forensic Sci. Int.* 179, 199–205

[112] Causin, V. *et al.* (2008) The discrimination potential of ultraviolet-visible spectrophotometry, thin layer chromatography, and Fourier transform infrared spectroscopy for the forensic analysis of black and blue ballpoint inks. *J. Forensic Sci.* 53, 1468–1473

[113] Wang, X.F. *et al.* (2008) Identification and dating of the fountain pen ink entries on documents by ion-pairing high-performance liquid chromatography. *Forensic Sci. Int.* 180, 43–49

[114] Xu, Y. *et al.* (2006) Dating the writing age of black roller and gel inks by gas chromatography and UV-vis spectrophotometer. *Forensic Sci. Int.* 162, 140–143

[115] Fischer, T. *et al.* (2022) Profiling and imaging of forensic evidence – A pan-European forensic round robin study part 1: Document forgery. *Sci. Justice* 62, 433–447

[116] Kunicki, M. (2002) Differentiating blue ballpoint pen inks. *Probl. Forensic Sci.* 51, 56–70

[117] Adam, C.D. (2008) In situ luminescence spectroscopy with multivariate analysis for the discrimination of black ballpoint pen ink-lines on paper. *Forensic Sci. Int.* 182, 27–34

[118] Khan, M.J. *et al.* (2018) Automated forgery detection in multispectral document images using fuzzy clustering. *Proc. - 13th IAPR Int. Work. Doc. Anal. Syst. DAS 2018*

[119] Reed, G. *et al.* (2014) Hyperspectral imaging of gel pen inks: An emerging tool in document analysis. *Sci. Justice* 54, 71–80

[120] Khan, Z. *et al.* (2013) Hyperspectral imaging for ink mismatch detection. *Proc. Int. Conf. Doc. Anal. Recognition, ICDAR*

[121] Wilkinson, T.J. *et al.* (2002) Use of synchrotron reflectance infrared spectromicroscopy as a rapid, direct, nondestructive method for the study of inks on paper. *Appl. Spectrosc.* 56, 800–803

[122] Silva, C.S. *et al.* (2013) Classification of blue pen ink using infrared spectroscopy and linear discriminant analysis. *Microchem. J.* 109, 122–127

[123] van Es, A. *et al.* (2009) Discrimination of document paper by XRF, LA-ICP-MS and IRMS using multivariate statistical techniques. *Sci. Justice* 49, 120–126

[124] Payne, G. *et al.* (2005) Visible and near-infrared chemical imaging methods for the analysis of selected forensic samples. *Talanta* 67, 334–344

[125] Hatzistavros, V.S. and Kallithrakas-Kontos, N.G. (2008) Trace element ink spiking for signature authentication. *J. Radioanal. Nucl. Chem.* 277, 399–404

[126] Maind, S.D. *et al.* (2008) Quantitative evaluation of europium in blue ballpoint pen inks/offset printing inks tagged with europium thenoyltrifluoroacetonate by spectrofluorometry and ICP-AES. *Sci. Justice* 48, 61–66

[127] Egan, W.J. *et al.* (2003) Forensic discrimination of photocopy and printer toners. III. Multivariate statistics applied to scanning electron microscopy and pyrolysis gas chromatography/mass spectrometry. *Anal. Bioanal. Chem.* 376, 1286–1297

[128] Merrill, R.A. *et al.* (2003) Forensic discrimination of photocopy and printer toners I. the development of an infrared spectral library. *Anal. Bioanal. Chem.* 376, 1272–1278

[129] Lennard, C. *et al.* (2015) Forensic application of laser-induced breakdown spectroscopy for the discrimination of questioned documents. *Forensic Sci. Int.* 254, 68–79

[130] Spigulis, J. *et al.* (2017) Method and device for smartphone mapping of tissue compounds, WO2017/012675A1

[131] Rubins, U. *et al.* (2017) Device for speckle-free imaging under laser illumination, WO 2017/025775 A1

ADDITIONAL INFORMATION

Participation in international schools:

1. "How to cross the "Valley of Death"; between research and the forensic market", Multiforesee summer school, online, 22.–24.06.2021.
2. "Biophotonics and imaging graduate summer school BIGSS 2020", online, 25.–29.08.2020.
3. "MultiForesee training school Operational CSI and Imaging Techniques" (COST action CA16101), Maastricht, Netherlands, 10.–14.12.2018.
4. "Biophotonics and imaging graduate summer school BIGSS 2018", Ballyvaughan, Ireland, 27.08.–2.09.2018.
5. "Biophotonics '17", Ven, Sweden, 10.–17.06.2017.

Popular scientific articles

1. J. Spīgulis, **I. Ošiņa**, "Spectral line imaging: principles, implementation and applications", Latvian Academy of Sciences, ***Yearbook-2022***, 98–101 (2022).
2. J. Spīgulis, **I. Ošiņa**, V.Lukinsone, U.Rubīns, "New optical methods have been developed at the Institute of Atomic Physics and Spectroscopy of the University of Latvia", ***Zinātnes Vēstnesis***, 1(606), 1–2 (2021)

Popular scientific presentations

1. Morning Panorama, "Skin health check in minutes. New facilities are being created in Latvia", 08.02.2021.
2. UL New Technologies & Innovations Day, Knowledge Agora, Riga, Latvia, presentation "Portable skin diagnostic device", I. Ošiņa, J. Spīgulis, U. Rubīns, Z. Rupenheits, M. Mileiko, 25.09.2020.
3. TV3 program "900 seconds", "A new device is being developed in Latvia, which will allow faster detection of malignant skin tumors", 16.01.2020.

Other publications

E. V. Plorina, D. Bliznuks, A. Lihachev, A. Derjabo, **I. Ošiņa**, I. Lihacova, M. Lange, "Optical design improvement for noncontact skin cancer diagnostic device", ***Proc. SPIE***, 10685, Biophotonics: Photonic Solutions for Better Health Care VI, 1068542, p. 147., (2018), doi: 10.1117/12.2307125.

Award

One of the most significant achievements in science in Latvia 2020: "A multispectral imaging method with a record high spectral selectivity has been developed and tested, which allows characterizing the optical and compositional characteristics of objects in detail without direct contact", J. Spīgulis, **I. Ošiņa**, U. Rubīns, E. Kviesis-Kipge, Z. Rupenheits, M. Mileiko

ACKNOWLEDGEMENTS

I want to express gratitude to my supervisor professor *Dr. habil. phys.* Jānis Spīgulis for involving me in the biophotonics field, for the given opportunities to improve my scientific career and for the great support and help throughout the preparation process of my thesis.

Thanks to the supportive colleagues at the Institute of Atomic Physics and Spectroscopy who helped with scientific advice and suggestions, programming, and various technical problems, as well as friendship, understanding and support. I would especially like to thank Edgars Kviesis-Kipge, Ilona Kuzmina and Uldis Rubīns for the excellent work atmosphere!

I would like to thank my family for their support and understanding throughout my studies. Special thanks to my sister Kristīne for her help, advice and encouragement and to my beloved Toms for his support and strength at the finish line of writing my dissertation. Thanks to Inga Pudža for her friendship and inspiration during all these years of studies.

The doctoral thesis has been developed by the financial support of several international and national projects: "Smart Materials, Photonics, Technologies and Engineering Ecosystem" (VPP-EM-FOTONIKA-2022/1-0001), "Strengthening of the Capacity of Doctoral Studies at the University of Latvia within the Framework of the New Doctoral Model" (UL No. ESS2021/434), "Multimodal imaging technology for in-vivo diagnostics of skin malformations" (UL No. ESS2019/314), "Advanced spectral imaging technology for skin diagnostics" (UL No. LZP2018/31), "Portable Device for Non-contact Early Diagnostics of Skin Cancer (Industrial research)" (UL No. ESS2017/190), "Biophotonics: imaging, diagnostics and monitoring" (UL No. ZD2014/29721), "Innovative imaging technologies for skin diagnostics" (UL No. ESS2014/159).

I am grateful to the COST action projects CA17121 "Correlated Multimodal Imaging in Life Sciences (COMULIS)" and CA16101 "Multi-modal Imaging of Forensic Science Evidence - tools for Forensic Science (MULTI-FORESEE)" for the opportunity to participate in international research.